2.4 HEAVY-ION DRIVER DESIGN AND SCALING

2.4.1 Introduction

A driver for an inertial fusion energy (IFE) reactor must deliver sufficient energy and power density to ensure target ignition. Although the requirements on efficiency and cost are less absolute, higher efficiencies and lower costs lead to more attractive plant designs.

In order to produce target ignition and gain, the driver must deliver several MJ of energy to a small spot size (approximately 2 to 4 mm in radius) in a very short-duration shaped pulse. The total pulse duration may be several tens of nanoseconds, but most of the driver energy should be delivered at the end of the pulse. The duration of the high-power part of the pulse may be less than half of the total pulse duration.

The fraction of an IFE plant's gross electrical power that must be recirculated to operate the driver is given by

$$f_R = \frac{1}{\eta_D G M_0 \eta_{th}}$$

where

f_R = recirculating power fraction,

η_D = driver efficiency,

G = target gain,

M_0 = energy multiplication factor of the blanket, and

η_{th} = thermal conversion efficiency.

Plant designs attempt to make all of these power ratios as large as possible, since it is difficult to achieve economic power production if f_R exceeds 20 to 25%. For the Osiris power plant, $M_0 = 1.25$ and $\eta_{th} = 45\%$. As we will show in this chapter, the base-case heavy-ion driver has an efficiency of 28% and produces a target gain of 86.5. This gives a small recirculating power fraction of ~ 7%.

It is also desirable to minimize the cost of the driver in order to keep the plant capital costs and cost of electricity (COE) competitive with the costs for power plants using other energy sources. The estimated cost of the driver described in this chapter results in a economically attractive power plant (see Chapter 8).

2.4.2 Heavy-Ion Driver Description

A heavy-ion induction linac for use as a driver for an IFE power plant will consist of: an ion injector, a multiple beam induction accelerator to produce high beam energies and currents, a drift compression region for shortening the ion bunch lengths, and a final focussing system for reducing the beam radii to the small spot size required for target ignition. Figure 2.26 shows a schematic diagram of a heavy-ion driver.

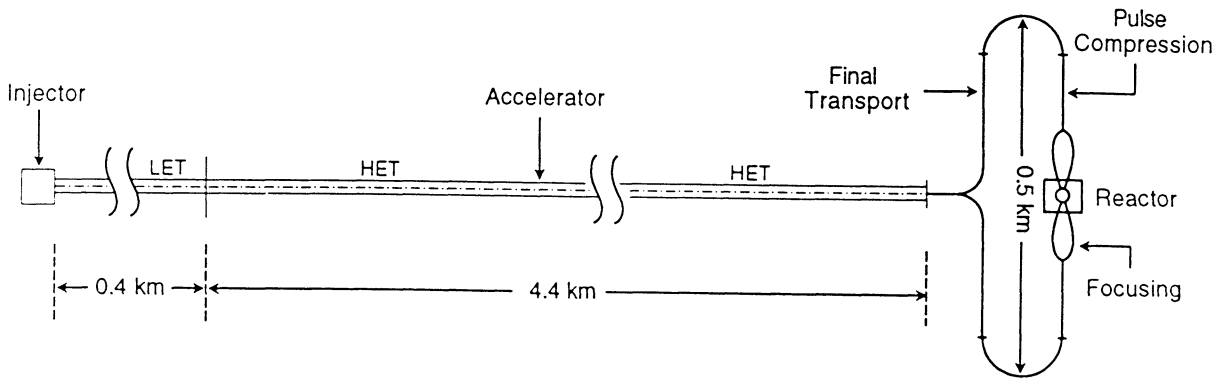

Fig. 2.26. Major elements of a heavy-ion driver.

The injector consists of a source of charged ions and a voltage gradient to accelerate the ions. The injector is followed by an injection matching section where the ion beam parameters (spot-size and undepressed tune) are adjusted to match those of the accelerator focusing lattice.

There are several types of sources and injectors. A simple injector could consist of a plasma-discharge ion source followed by a voltage grid. In this design, ions would be created from a gas or vapor by a discharge voltage and then accelerated between electrical voltage grids. The shape of the grids (anodes and cathodes) is designed to produce a source of ions with minimal angular divergence. We have not created a detailed design of the injector, but we have used common limits to scale the achievable injection currents with ion mass, ion charge state, and acceleration gap voltage.

The accelerator consists of a lattice of quadrupole arrays with induction cells located between the arrays. The quadrupole arrays contain a superconducting quadrupole winding around each beam tube. The quadrupole field of adjacent quadrupoles are offset by a 90° rotation to provide an alternating focusing lattice (which is described as a focusing-drift-defocusing-drift, or FODO, lattice). Each pair of quadrupoles in a repeating FODO lattice focuses the beam in two dimensions. Inductor cells are placed between quadrupoles as shown in Fig. 2.27 Each induction cell consists of a ferromagnetic core surrounding all of the beams as shown schematically in Fig. 2.28; the cores accelerate the beams through transformer action.

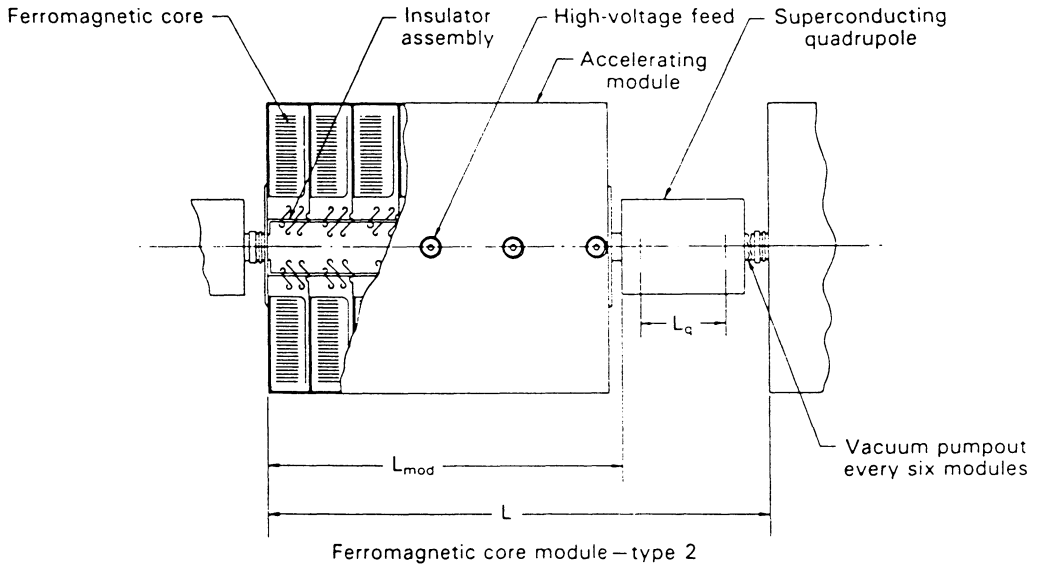

Fig. 2.27. Acceleration and focusing components in each half-lattice period.[2.37]

Because of the need for very short pulse durations at the target, the axial length of the pulse must be compressed after the beam leaves the accelerator. This is done by using a shaped pulse for the final induction cells to preferentially accelerate the end of the ion pulse and give the beams a velocity tilt. The drift compression region follows the final inductors and allows the velocity tilt to compress the beam's length.

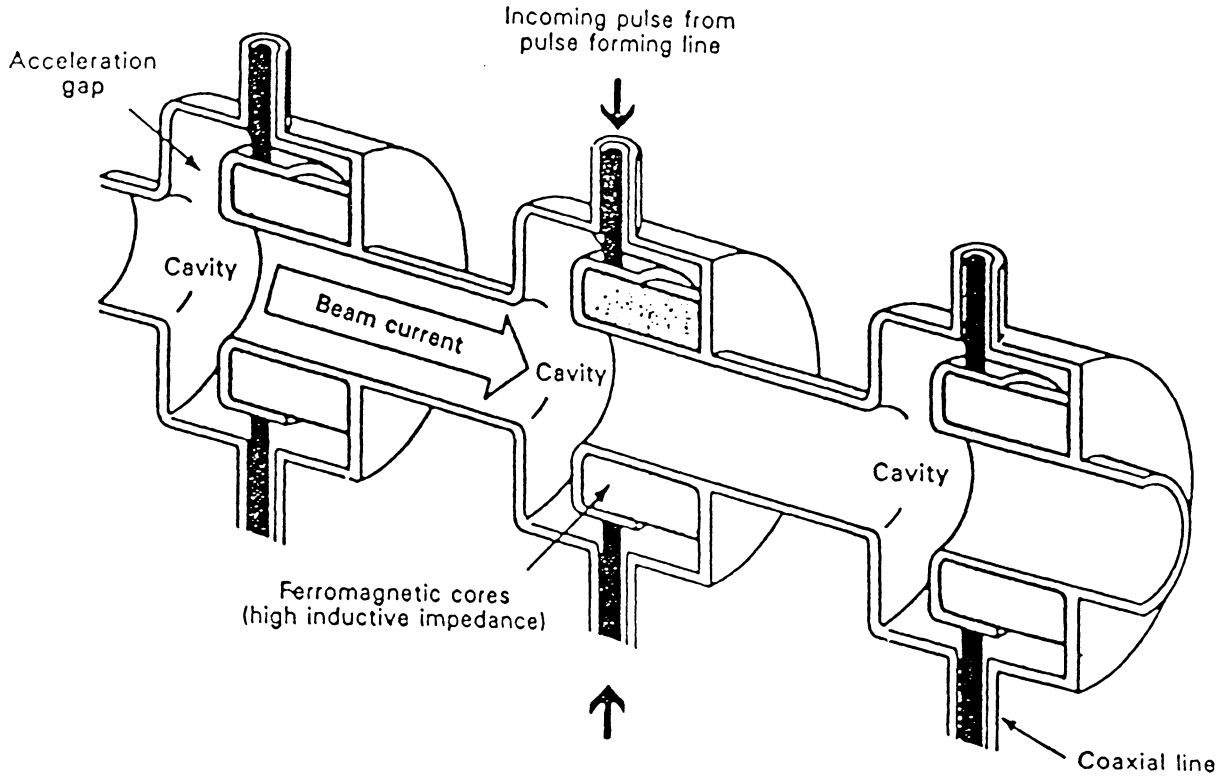

Fig. 2.28. Schematic cutaway of an induction linac.[2.38]

The final focusing system consists of quadrupole pairs or triplets which compress the beams to the final spot size. In order to attain the smallest possible spot sizes, the beams are separated and expanded before final focusing. The beams are also neutralized with co-injected electrons just after leaving the final focusing magnets in order to minimize space-charge effects during focusing.

2.4.3 Design Strategy

Our design strategy builds upon one described by Monsler[2.39] in 1987. The chosen high-energy propagation mode uses a constant effective focusing length for each quadrupole and a constant beam radius. This allows for a single quadrupole array design to be used for the entire length of the driver. The spacing of the quadrupole arrays (the linear quad packing fraction) is varied so that the beam carries the maximum allowable current at every point in the driver.

Two types of inductor cells are used. A large radial build is used in the beginning of the driver where cores and quad arrays are packed closely together, and a smaller radial build is used in the high-energy section of the driver where there are greater separations between quad arrays. The use of inductors with a smaller radial build in the longest section of the driver lowers the total required volume of core material (metglas).

The use of a single design for the quad arrays and only two designs for the inductors simplifies manufacturing requirements and allows for maximum economy of scale for producing driver components.

Our reference design is conservative in several respects. More aggressive driver designs use beam combination, beam separation, and/or recirculation to lower driver costs. All three modifications add performance uncertainties and design complexity, so we have chosen not to use these options in our base driver. We also chose a base design using singly charged, $q = 1$, ions. Higher charge states require more complicated sources and injectors, and highly charged ions may require better vacuums because of the increased potential for beam-gas charge exchange.

Beam combination could reduce the length and cost of the low-energy part of the driver. If beams can be combined, then high beam currents can be achieved early in the driver without large beams or unattainable rates of pulse compression. Unfortunately, even perfect theoretical beam combination leads to beam emittance growth which degrades target performance.

Beam separation before final focusing could theoretically lower the emittance per beam and reduce the achievable single-beam spot sizes. The beam separators would have to split beams with the high final ion energies and currents at the end of the accelerator with minimal beam loss. Even small amounts of ion loss may be disastrous at final beam energies. Any ions "lost" from the front of the pulse will impact the beam tube and scatter ion and electrons from the wall that may interfere with the following ions. While it is possible that the required beam separators could be developed, we have not assumed them in our base design.

Recirculation involves bending sections of the driver into a circle so that the beam may pass through each acceleration cell several times. Recirculation can greatly reduce the number and cost of driver components required, but the feasibility of recirculation has not yet been demonstrated. Critical issues include the effects of bending magnets on beam quality (emittance),

maintaining vacuum quality in the beam lines over several beam "laps", and the possibility for several modes of resonant instability growth.

2.4.4 Accelerator Modeling

Each driver is designed from both ends. The beam parameters in the majority of driver are set by the desired final beam energy and pulse duration. The beam parameters, required energy, and length of the low-energy transport stage are set by the injector beam parameters for a beam radius consistent with the beam radius and total charge used in the high-energy transport section of the driver. An intermediate pulse-matching stage is inserted between these two driver sections in order to shorten the pulse length (and thus increase the current) coming from the low-energy stage to that needed for the high-energy stage.

The three heavy-ion driver stages can be described as a low-energy transport stage, a pulse-matching stage, and a high energy transport stage. In the low-energy transport stage, initial beam currents and pulse lengths are determined by injector characteristics, and acceleration gradients and pulse compression are limited by the velocity tilt limit for the magnetic focusing lattice. The velocity tilt limit results from the fact that charged particles with different velocities in a given magnetic field experience different forces. Even though the single-particle trajectories in a quadrupole lattice are independent of velocity (since displacements in a constant magnetic field gradient are set by the charge-to-mass ratio), the head-to-tail relative velocity difference ($\Delta v/v$) for the beam must be limited to prevent serious mismatch oscillations of the beamlets in the focal system.

In the pulse-matching stage, the acceleration gradient is fixed at the insulator flash-over limit and pulse compression continues at the velocity tilt limit. The flash-over limit for a beam-tube is much lower than the hold-off voltage gradient for the beam-line vacuum. If the average acceleration gradient along the beam-tube is high enough, a charged particle released near the tube wall will accelerate, impact the wall, release more particles, and produce a discharge breakdown of the applied electric field. Because the allowable acceleration gradient at injection is well below the flash-over limit, the gradient is continuously increased in the low-energy transport stage. Once the flash-over limit is reached, the average acceleration gradient must remain constant, but head-to-tail acceleration differences can still be used for pulse compression.

The need for a pulse-matching stage could be removed if larger injector voltages, larger injector currents, or larger beam diameters for the low-energy stage were used.

The high-energy transport stage makes up most of the accelerator (roughly 90% of the total length). During the high-energy stage, the physical pulse length is kept constant and the voltage gradient remains fixed at the insulator flash-over limit; the scaling of beam parameters in this section was first described in Monsler's 1987 paper.

2.4.4.1 Scaling High-Energy Beam Parameters from Final Beam Requirements

The Maschke equations[2.40] can be used to determine the maximum transportable beam current, I_b, as a function of the cumulative acceleration voltage, V. The relationship between achievable final beam current and final driver voltages can then be used to determine the minimum driver voltage needed for a given driver power (driver energy / final accelerator pulse duration). The Maschke limits for beam current and beam radius can then be used with the constant voltage gradient to determine the beam parameters throughout the high-energy driver stage.

The Maschke equations derive the transportable current and beam size by equating the focusing force given by the continuous limit approximation for FODO focussing systems with the defocusing forces resulting from a given line charge density. The Maschke limit for the beam current is

$$I_b = (2.89\ \mathrm{MA}) \left(1 - \left(\frac{\sigma}{\sigma_0}\right)^2\right) \left(\sigma_0^4\, (\beta\gamma)^5\, \eta^2 \left(\frac{A}{q}\right) \left(\frac{\varepsilon_n}{\sigma}\right)^2 B_{be}^2\right)^{1/3}$$

where

A = the ion mass (amu),

q = the ion charge state,

B_{be} = the maximum magnetic field at the beam edge (T),

ε_n = the normalized emittance of the beam (m-radians),

η = the axial quad packing fraction (η_i is η at injection),

σ_0 = the undepressed tune (phase advance per lattice period in radians),

σ = the depressed tune (including space charge effects) (radians), and

$\beta\gamma$ = relativistic factor approximately given by

$$\beta\gamma = \left[\sqrt{\frac{2\,q\,e}{A\,m_p\,c^2}}\right]\sqrt{V}$$

In order to maintain a constant beam radius, the axial packing of the quadrupole fields must scale as $\eta = \eta_i\,(V_i / V)^{1/2}$. Using this relationship gives the desired equation for the maximum transportable beam current as a function of cumulative voltage

$$I_b(V) = 2.89 \times 10^6 \left(1 - \left(\frac{\sigma}{\sigma_0}\right)^2\right)\left(\sigma_0^4\,\eta_i^2\,V_i\,\frac{A}{q}\left(\frac{\varepsilon_n}{\sigma}\right)^2 B_{be}^2\right)^{1/3}\left(\frac{2\,q\,e}{m_p\,A\,c^2}\right)^{5/6}\sqrt{V}$$

or

$$I_b(V) = C_I(\eta_i,\ B_{max},\ A,\ q,\ \sigma,\ \sigma_0,\ \varepsilon_n,\ V_i)\ \sqrt{V}$$

where, in addition to the variables already defined,

C_I = constant that depends on the indicated parameters,

m_p = the mass of a proton (nucleon) in kg,

e = the charge of an electron in Coulombs,

V_i = the injection voltage in Volts, and

B_{max} = 1.5 B_{be} is the Max. field at the Superconductor.

The required accelerator voltage can then be found from the driver energy, E, and the post-acceleration pulse duration, τ_f by solving the following power equation for V:

$$V\,I_b(V) = \frac{E}{N\,\tau_f}$$

where N = number of beams and τ_f is the pulse duration of the beam as it leaves the accelerator. The required final voltage is thus:

$$V_f = \left(\frac{E}{N\,\tau_f\,C_I}\right)^{2/3}$$

and the required final beam current is given by: $I_{b,f} = I_b(V_f)$. The decision to fix the beam radius, the effective quadrupole length, and the undepressed tune also fixed the physical pulse length and the depressed tune as constant.

Figures 2.29a and 2.29b show the calculated accelerator voltages and beam currents as a function of driver energy for heavy-ion drivers using our base parameters. The chosen base-driver parameters were the result of a parametric study described in Section 2.4.8. The base driver parameter set was: N = 12 beams, τ_f = 100 ns, η_i = 0.8, B_{max} = 10 T, A = 131, q = 1, σ = 8°, σ_0 = 80°, and $\varepsilon_n = 10^{-5}$ meter - radians, for an assumed injection voltage of V_i = 3 MV.

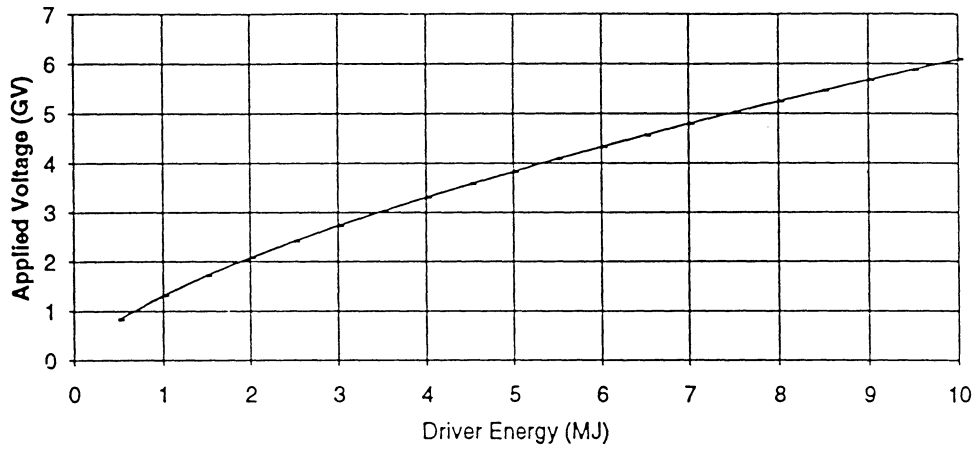

Fig. 2.29a. Cumulative voltage for base driver designs.

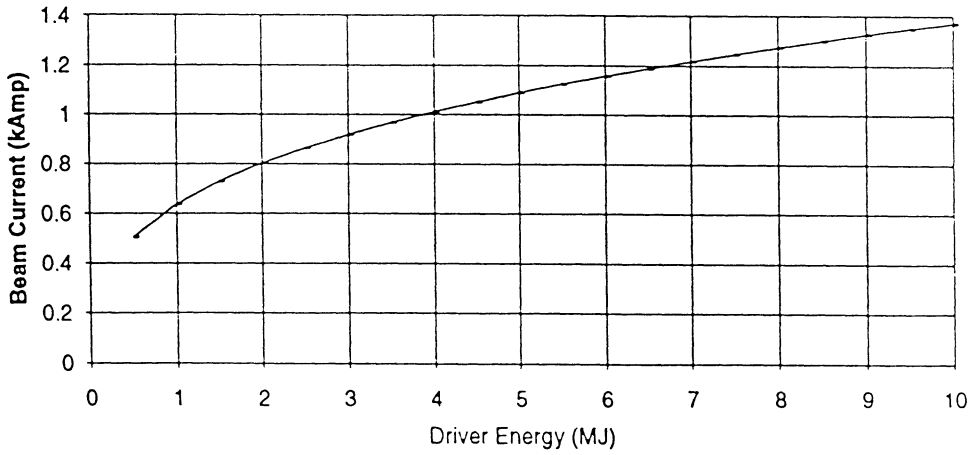

Fig. 2.29b. Final beam currents for base driver designs.

2.4.4.2 Ion Range, Spot Size, and Target Gain

Once the final beam voltage and current are determined, the gain and optimum final focusing half angle can be scaled from the corresponding ion range, R_{ion}, and spot size, r_s. For this study, we developed the following curve fit for cold ion ranges in terms of the ion mass, A, and cumulative accelerator voltage, V:

$$R_{ion} = \left(3.04 \times 10^{-5} A + 349\, A^{-2.21}\right) \left(\frac{qV}{10^9}\right)^{(1.72 - 0.00275A)} \text{ g/cm}^2.$$

Figure 2.30 shows the ion range as a function of energy for our base driver parameters.

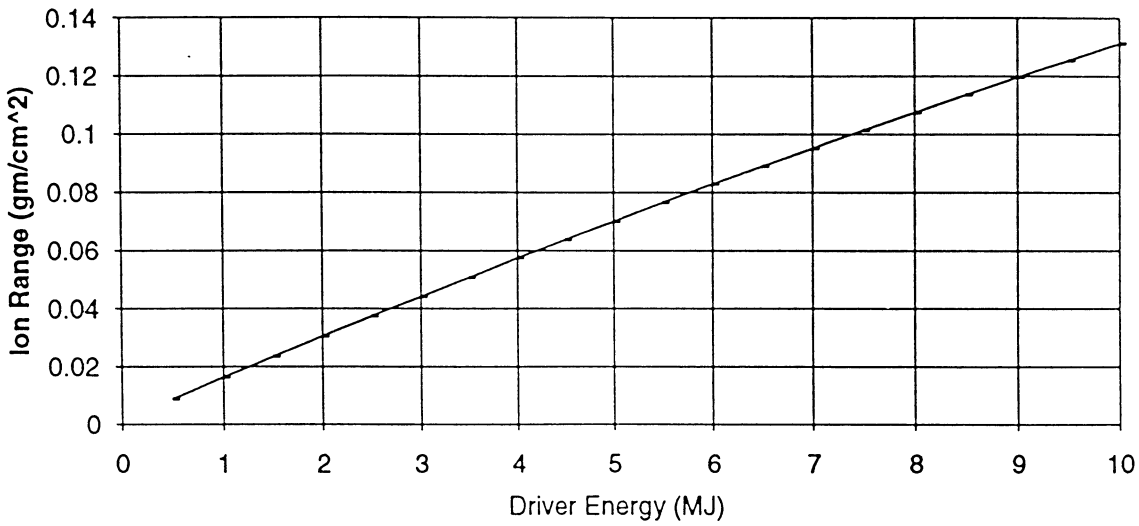

Fig. 2.30. Ion ranges for base driver designs.

The achievable spot size depends on the final focusing half angle, θ. We elected to specify θ for each driver as that value yielding the minimum spot size, r_s. The spot size, r_s, is determined as discussed in Section 2.4.7.2. Figure 2.31 shows the minimum spot size vs. energy for our base parameters, and Fig. 2.32 shows the dependence of spot size contributions on the final focusing half angle for a 5 MJ driver.

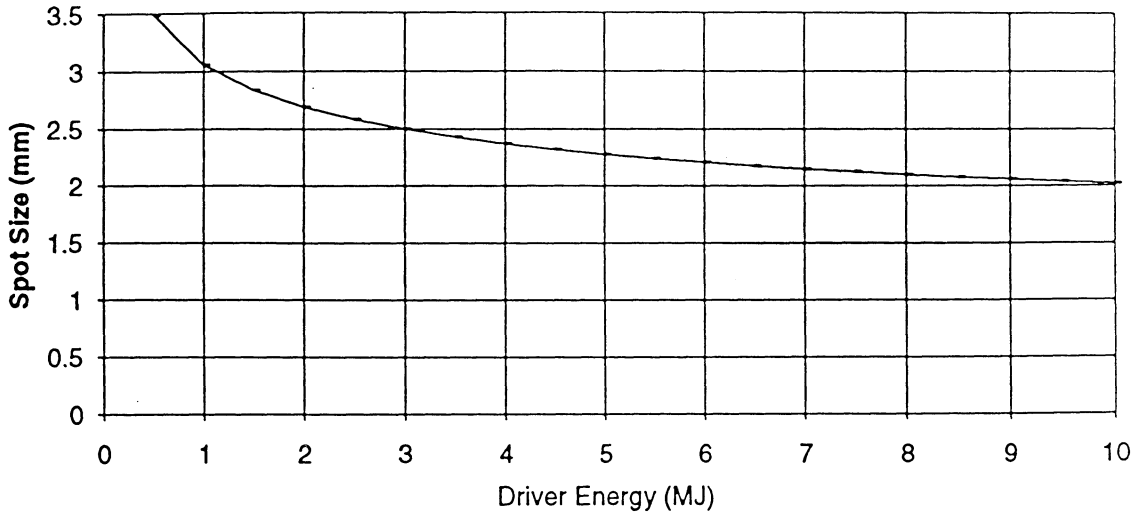

Fig. 2.31. Spot sizes for base driver designs.

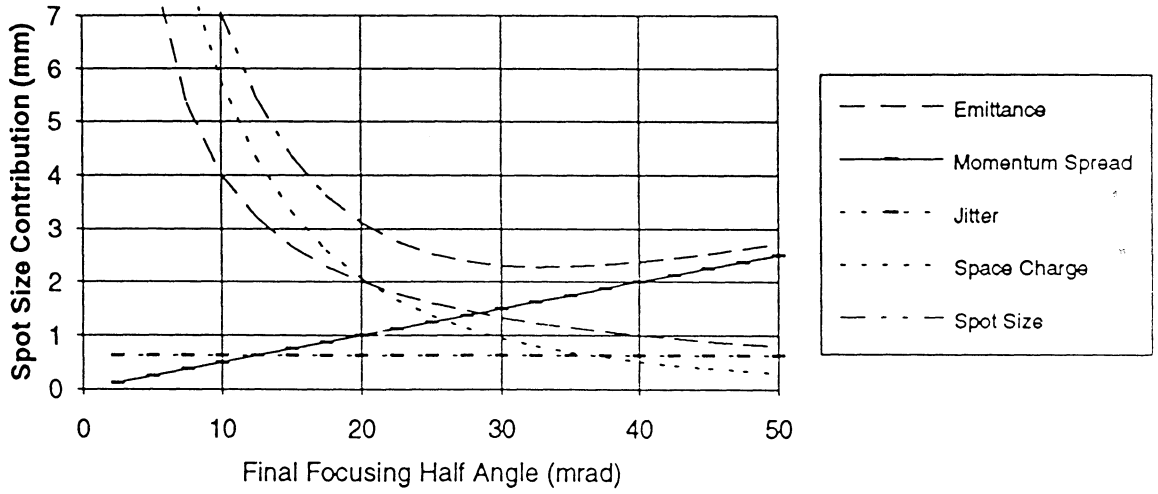

Fig. 2.32. Spot size contributions for a 5 MJ heavy-ion driver.

Gain curves for indirect drive targets provided by the study guidelines were fit to the functional form G = A + B ln(E), where A and B are functions of r_s and R_{ion}. The resulting gain calculations:

$$G = 62.6 - 142.3\, r_s^{1.25} R_{ion}^{0.633} + \left(32.8 + 82.1\, r_s\right)^{0.783} R_{ion}^{0.647} \ln(E)$$

(where E is given in MJ) are shown as a function of E for our base driver in Fig. 2.33.

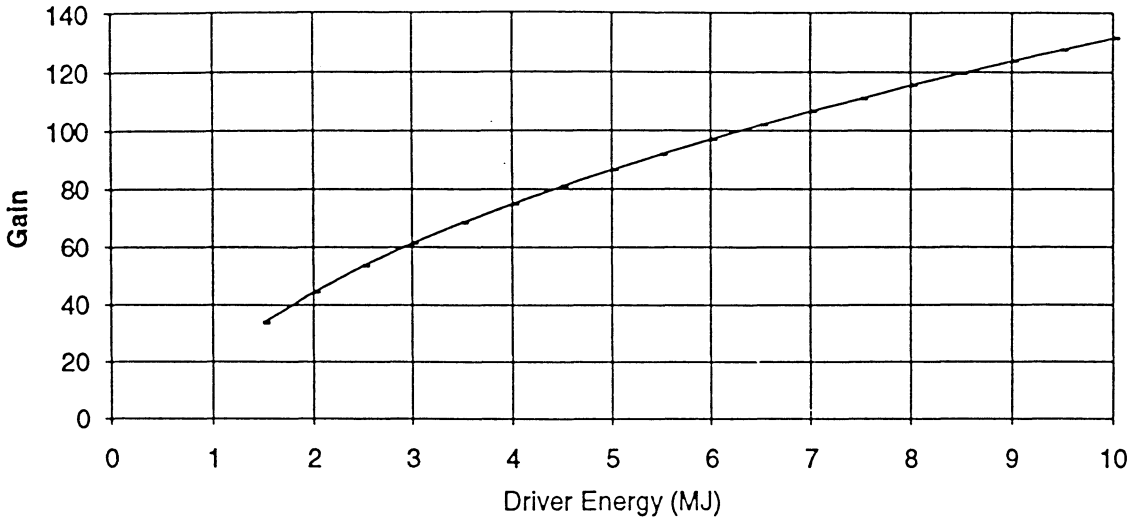

Fig. 2.33. Gain curve for base driver designs.

2.4.4.3 Injector Characteristics

A detailed injector design was beyond the scope of this study. The base injector design and scaling shown here were taken from the HIFSA study.[2.41] More advanced injector designs may be able to produce higher injection currents and/or higher energy ions.

The injected current density is assumed to be limited by the Child-Langmuir law:[2.42]

$$j = 5.46 \times 10^{-8} \sqrt{\left(\frac{q}{A}\frac{V_s^3}{d^4}\right)}$$

where

V_s = (4/3) V_i = the extractor voltage (assumed = 4 MeV for all drivers), and

d = the source extraction gap width (= 0.8 m for a 5 MV/m voltage gradient limit).

In order to increase the injection current, the source radius can be larger than the transport beam radius (a). Assuming focusing in the injector which allows a source radius of 2×a, gives an injected current per beam, $I_{b,inj}$, of:

$$I_{b,inj} = 4\pi a^2 \left[5.46 \times 10^{-8} \sqrt{\frac{q}{A}\frac{V_s^3}{d^4}}\right]$$

Where the transport beam radius is given by the Maschke approximation:

$$a = (2.32\ \mathrm{m}) \left[\left(\frac{\sigma_0}{\eta} \right) \left(\frac{1}{\beta\gamma} \right) \left(\frac{A}{q} \right) \left(\frac{\varepsilon_n}{\sigma} \right)^2 \left(\frac{1}{B_{be}} \right) \right]^{1/3}$$

which is a simplified version of the approximation:

$$a = \left[\frac{\varepsilon_n^2 \sigma_0 c^2}{\sigma^2 \left(\frac{B_{max}}{1.5} \right) \eta_i \sqrt{V_i}} \right]^{1/3} \left[\frac{2 A m_p}{q e} \right]^{1/2}$$

Assuming 8% of the beam is lost from the injector to the target (a somewhat arbitrary assumption allowing for 2% beam loss in the injector, 2% beam loss in the accelerator, 2% beam loss in final focussing, and 2% beam loss in the chamber), the pulse duration at injection will be:

$$\tau_i = \frac{Q_{inj}}{I_{b,inj}} = \frac{1}{0.92} \frac{\tau_f I_{b,f}}{I_{b,inj}}$$

where $I_{b,f}$ is the final beam current calculated earlier. The corresponding pulse length will be:

$$l_{p,inj} = \tau_i \sqrt{\frac{2 q e V_i}{A m p}}$$

Possible Improvements in Injector Performance. Both The cost and performance of a heavy-ion driver improve significantly with increases in the assumed injector voltage and current. The injected current limit from the Child-Langmuir law is a small fraction of the transportable current limit for the focusing lattice. In theory, an injector could be built with current densities much greater than those given by the Child-Langmuir law. High injected currents and injector voltages are not assumed in our designs because high voltage, high current density injectors require significant development.

An example of a high current injector would be a low-voltage, high-current, converging beam source followed by a long low-gradient (10 kV/cm) acceleration column with quadrupole

pairs for focusing the beam to the desired beam size. Advanced injectors such as this could provide currents and beam sizes closer to the transport limits of the quadrupole focusing array.

Producing a high-current, low-emittance beam and matching the beam parameters to those required by the accelerator is a complex problem. A source producing converging ions requires an acceleration gap with shaped electrodes.

If the injector current can be increased enough so that the initial current limit is set by the transport lattice, the limits on the transportable current will need to be examined more closely. The Maschke limit assumes step-like quadrupole fields which have constant strengths over an effective length. Actual magnets will have to be longer than their effective field lengths, and field cancellation from the end fields of adjacent magnets may further limit the maximum axial packing fraction for the quadrupole fields. These limits on η become less important at high energies where η is small, but both limits could reduce the allowable low-energy currents below our calculated currents.

Transportable currents at low ion energies may be increased by substituting electrostatic quadrupoles (such as those used at LBL in the MBE-4 experiment) for the magnetic quadrupoles. Short quadrupole designs and high axial packing fractions are much easier to achieve with electrostatic quadrupoles. However, because electrostatic quadrupoles use space-charge effects instead of magnetic fields, they are only effective for low line-charge density beams (i.e., at low beam currents).

2.4.4.4 Low-Energy Transport Modeling

Magnetic focusing requires a maximum velocity tilt,

$$\left(\frac{V_{tail} - V_{head}}{V_{ave}}\right)$$

of 0.3 . In order to prevent elongation of the pulse, the entire pulse is loaded into the accelerator before acceleration is begun; this gives a limit on the initial voltage gradient, Φ_i (Volt/m), of:

$$\Phi_i = 0.3 \frac{V_i}{I_{p,inj}}$$

The allowed voltage gradient will then increase as:

$$\Phi(V) = \Phi_i \left(\frac{V}{V_i} \right)^{3/2}$$

where V is the cumulative accelerator voltage, until the insulator flash-over limit is reached. Once the flash-over limit is reached, the acceleration gradient remains constant for the remainder of the driver.

2.4.4.5 Pulse Compression in the Pulse-Matching Driver Stage

The pulse length is fixed at injection by the injector current density limits and is fixed at the end of the accelerator by the choice of desired beam power (E and τ_f are set). Because we have chosen to keep the pulse length constant during high-energy transport, we need to adjust the pulse length at the end of the low-energy stage of the driver to the desired final value. In almost all cases, additional pulse compression is required after the low-energy stage. This pulse compression can be done by using a shaped pulse on the inductor cells which has an average voltage determined by the voltage flash-over limit and increasing voltage as the pulse passes through the inductor.

Because the pulse duration of the beam varies as the inverse of the cumulative voltage in the low-energy driver stage, the pulse duration at the end of the low-energy stage, τ_{fo} will be

$$\tau_{fo} = \tau_{inj} \frac{V_{inj}}{V_{fo}}$$

where V_{fo} is the voltage at which the voltage gradient (determined by the velocity tilt limit) reaches the insulator flash-over limit, Φ_{fo} = 0.85 MV/m (this limit is actually the product of the insulator limit of 1 MV/m and the fraction of the driver axial length lined with insulator = 0.85). V_{fo} can be calculated from the acceleration gradient limit given earlier as

$$V_{fo} = \left[\frac{\Phi_{fo}}{\Phi_i} \right]^{2/3} V_{inj}$$

so the pulse length at the end of the low-energy stage will be given by

$$l_{p,fo} = \tau_i \frac{V_i}{V_{fo}} \sqrt{\frac{2qeV_{fo}}{Am_p}}$$

The pulse length during the high-energy stage of the driver is equal to the final pulse length, $l_{p,f}$, which is determined by the final voltage of the accelerator, V_f, and the final pulse duration, τ, from the relationship

$$l_{p,f} = \tau_f \sqrt{\frac{2qeV_f}{Am_p}}$$

Because pulse compression is done at a velocity tilt limit of $\Delta v/v = 0.3$, the required length for the pulse compression region, X_{pc}, is then:

$$X_{pc} = \frac{1}{0.3} (l_{p,fo} - l_{p,f})$$

The total accelerating voltage of this section can be obtained by multiplying X_{pc} by Φ_{fo}.

2.4.4.6 Summary of Beam Parameter Scaling in the Three Driver Stages

Table 2.19 summarizes the dependencies described in the previous chapters for beam parameters variations in each driver stage with the cumulative accelerator voltage, V.

2.4.4.7 Requirements for Inductors and Quad Arrays

Quad Array Cross Section. Figure 2.34 shows the array and inductor cross sections, as well as a detailed cross section of the quadrupole insert. The required dimensions for quadrupole windings and the collar thickness are calculated from the quadrupole bore radius, the required magnetic field, and the properties of the superconductor and the collar material.[2.43] The compact arrays modeled allow some of magnetic field lines leaving one quadrupole to pass through adjacent quadrupoles. Designing high-field-quality windings for such an array is a complex problem, but the required dimensions will be similar to those of the simple windings modeled here. Parametric studies were done using steel collars around NbTi and Nb_3Sn superconducting windings with a 1:1 ratio of superconductor to copper.

Table 2.19. Scaling of Beam Parameters with Accelerator Voltage

	Low-Energy Stage	Pulse Matching Stage	High Energy Stage
Voltage	V_i to V_{fo}	V_{fo} to V_{HET}	V_{HET} to V_f
Voltage Gradient, Φ =	$\Phi_i \left(\frac{V}{V_i}\right)^{3/2}$	Φ_{fo}	Φ_{fo}
Beam Current, I_b =	$I_{b,inj}\left(\frac{V}{V_i}\right)$	$I_{b,fo}\left(\frac{l_{p,fo}}{l_p}\right)\sqrt{\frac{V}{V_{fo}}}$	$I_{b,f}\sqrt{\frac{V}{V_f}}$
Pulse Duration, τ =	$\tau_i\left(\frac{V_i}{V}\right)$	$\tau_{fo}\left(\frac{l_p}{l_{p,fo}}\right)\sqrt{\frac{V_{fo}}{V}}$	$\tau_f\sqrt{\frac{V_f}{V}}$
Pulse Length, l_p =	$l_{p,inj}\sqrt{\frac{V_i}{V}}$	$l_{p,fo} - \frac{0.3}{\Phi_{fo}}(V - V_{fo})$	$\tau_f\sqrt{\frac{2qeV_f}{(Am_p)}}$
Length of Stage in Base Driver	356 m	33.5 m	4.41 km

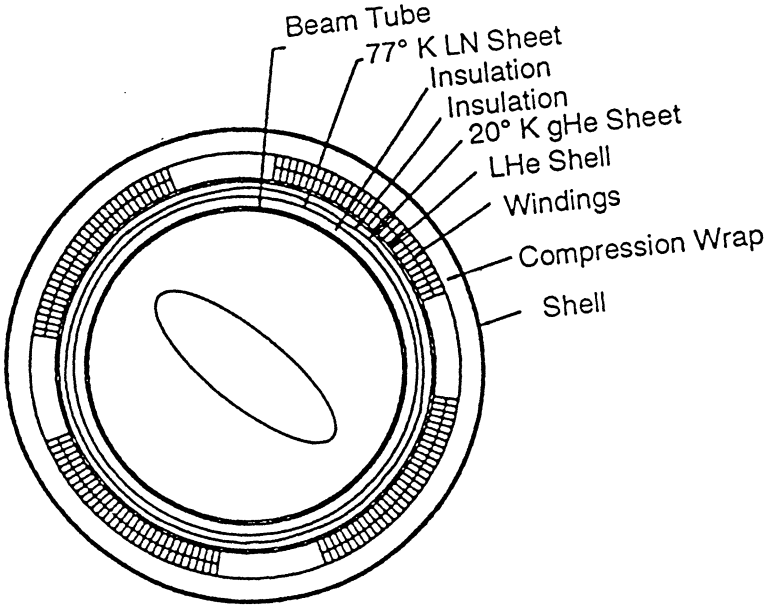

Quadrupole Insert

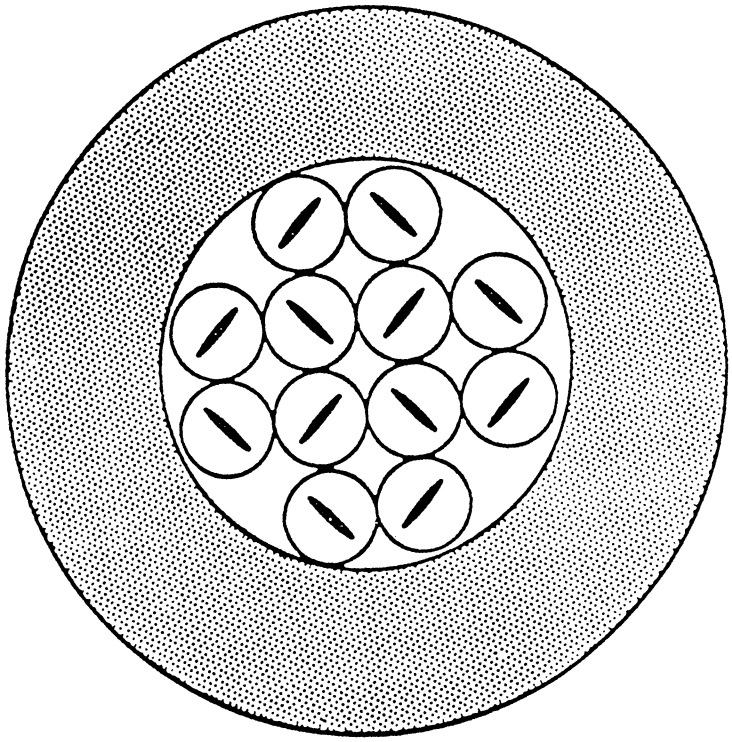

Fig. 2.34. Beam quad array and inductor cell cross sections.

Inner Winding Radius. The inner radius of the superconducting windings is set to 1.5 times the beam radius. This scaling allows for an inner beam tube radius roughly 1.3 times the beam radius surrounded by a 2 mm thick (warm bore) beam tube, 1 cm total thickness of superinsulation in three layers, two thin (mm) cooled Cu sheets at 77 K and 20 K, and a 2 mm thick support tube for the windings. These assumptions are based on the desire to keep the insulation and cooling dimension as small as possible while providing sufficient protection for the superconductors.

Winding and Collar Thickness. A quadrupole field requires a cos(2θ) current distribution, which may be approximated with four evenly spaced blocks of constant current (in alternating directions), each occupying a 60° arc with constant winding thickness. Actual windings will need to give better quality quadrupole fields and could consist of two or three radial layers each containing from one to three coils per quadrant, but the total required total thickness and conductor area will not differ greatly from the simpler model. The thickness is then given by:

$$\Delta R_w = R_{iw}\left[\exp\left(\frac{\pi}{\sqrt{3}}\,\frac{B}{\mu_0 \lambda J_c(B)}\,\frac{1}{R_{iw}}\right) - 1\right]$$

where:

- B = B_{max} = maximum magnetic quadrupole field (Tesla),
- R_{iw} = inner winding radius,
- λ = area fraction of the winding containing superconductor, and
- $J_c(B)$ = critical current of the superconductor.

The approximations used for $J_c(B)$ are:

$$J_c(B) = (3{,}520 - 339\,B)\left(\frac{MA}{m^2}\right)$$

for NbTi, and

$$J_c(B) = \frac{9.31 \times 10^4}{\sqrt{B_c}}\left(\left(1 - \left(\frac{T}{18.3}\right)^2\right)\left(1 - \frac{B}{B_c}\right)\right)^2\left(\frac{MA}{m^2}\right)$$

for Nb_3Sn,

where $B_c = 27.5\left(1 - (T/18.3)^2\right)(1 - T/54.9)$ is a function of the temperature, T (K).

The required collar thickness can then be determined from both the hoop stress if support from the array structure is assumed to cancel the bending moments. For a given collar thickness, t_c, the maximum hoop stress can be estimated by modeling the $\cos^2(2\theta)$ force distribution as four point loads on a ring.[2.44] This gives a maximum tensile load of

$$T = \frac{F}{2}\,\frac{1}{\sin(\pi/4)} = \frac{\left(B^2/(2\,\mu_0)\right)(\pi/4)\,R}{2\sin(\pi/4)}$$

The collar thickness is then set such that the tensile stress is less than half the yield stress of the collar material. The array is then scaled using trigonometric relationships for the radius of a circular "pile" of cylindrical quadrupoles with shaped iron inserts in the gaps, and a 2 cm thick steel collar around the entire array.

2.4.4.8 Required Length and Number of Driver Components

Core Requirements. The total magnetic flux, Φ_M (measured in Volt-seconds), required in each stage is obtained by integrating the pulse duration, $\tau(V)$, over V. Because the pulse duration, τ, continually decreases as the cumulative voltage, V, increases, the resulting requirements for each stage are:

$$\Phi_{M,\,LET} = \tau_i\,V_i\,\ln\left(\frac{V_{fo}}{V_i}\right)$$

for the low-energy stage,

$$\Phi_{M,\,PM} = 2\,\tau_f\sqrt{V_f}\left(\sqrt{V_{HET}} - \sqrt{V_{fo}}\right)$$

for the pulse-matching stage, and

$$\Phi_{M,\,HET} = 2\,\tau_f\,V_f\left(1 - \sqrt{V_{HET}/V_f}\right)$$

for the high-energy stage.

Each core can provide a volt-second impulse of: $\Phi_{M,\,core} = \Delta B\,\Delta r\,\Delta l$, where ΔB is the field swing of the core material (assumed = 2.4 T for metglas), Δr is the radial thickness of the core, and Δl is the axial width of the core. The number of cores needed in each section is then determined by the core dimensions, and the total volume of metglas can be calculated from these dimensions and the bore radius of the core. In the first two stages of the driver (LET and PM), the arrays intrude into the bores of the inductor cells, the bore radius is set to 1.05 times the outer quad array radius, Δr is set to 0.8 m, and Δl is set to 0.2 m. In the last stage of the driver, the arrays fit between adjacent inductor cells and the bore radius is set to 1.05 times the distance from the array center to the outermost beam tube, Δr is set to 0.4 m, and Δl is set to 0.1 m.

Quad Requirements. The total length needed for the quadrupole focusing fields, L_{focus}, can be obtained by integrating η/Φ with respect to V for each stage. The number of quadrupole arrays needed can then be obtained by dividing L_{focus} by the effective length of each quadrupole, L_q, where

$$L_q = \left(\frac{\varepsilon_n \eta_i \sigma_0^2 c \sqrt{V_i}}{\sigma B^2} \right)^{1/3} \sqrt{\frac{2 A m_p}{q e}}$$

In the low energy stage, the integral for L_{focus} gives:

$$L_{focus} = \eta_i V_i \left(1 - V_i/V_{fo}\right)/\Phi_i$$

The total focusing field length needed for the two higher-energy stages, where the voltage gradient is constant, is

$$L_{focus} = 2\,\eta_i \sqrt{V_i} \left(\sqrt{V_f} - \sqrt{V_{fo}}\right)/\Phi_{fo}$$

Total Driver Length. The total driver length can be obtained by integrating $1/\Phi$ from the injection voltage to the final voltage. This gives a driver length of:

$$L_{driver} = 2\,V_i \left(1 - \sqrt{V_i/V_{fo}}\right)/\Phi_i + \left(V_f - V_{fo}\right)/\Phi_{fo}$$

Quad Array and Inductor Costs. In choosing a base set of driver parameters, only the costs of the inductor cores and the quadrupole arrays were considered; total driver costs for our base driver are discussed in Chapter 8. Once the amount of materials needed in the arrays were calculated, the array components were priced using: \$300/(kg of superconductor in the windings), \$50/(kg of Cu in the windings), \$10/(kg of iron in the array), and \$25/(kg of steel in the collars). The inductor cores were priced using an assumed future unit cost of \$5/kg for metglas.

Because the inductor costs are larger than the quadrupole costs, minimizing material costs also implies minimizing the inductor core volumes. Minimizing the core volume also minimizes the energy lost in the cores and ensures that the chosen design is still optimal for more conservative assumptions on the price of metglas or the assumed cost/Joule of pulse forming networks (PFNs).

2.4.5 Driver Efficiency

Driver efficiency is calculated from energy losses in the pulse forming network and in the metglas inductor cells, and from energy given to the beam by each core. The voltage across a given cell is limited by the volt-seconds of the cell and the total time of pulse, this gives an energy gain per cell of $E_{beams}(V) = (N Q_{beam}) \frac{\Phi_{M,core}}{\tau(V)}$, or $E_{beams}(V) = N \Phi_{M,core} I_{beam}(V)$. The energy lost in the inductor core is scaled from the J/m^3 metglas losses,[2.45]

$$E_{loss}(V) = 140 \frac{(\Delta B)^{1.8}}{(\tau(V) \cdot 10^6)^{0.8}}$$

where τ is in seconds. The pulsed efficiency for a given inductor, η_p, is then given by

$$\eta_p(V) = \frac{E_{beams}(V)}{E_{beams}(V) + E_{loss}(V)}$$

and the average efficiency for the pulsed power is then

$$\langle \eta_p \rangle = \frac{1}{V_f - V_i} \int_{V_i}^{V_f} \eta_p (V)\, dV$$

The wall plug driver efficiency, η_{driver} , can be obtained from η_p, the pulse forming network efficiency (η_{pfn}), the driver energy (E), the driver repetition rate (ω), and the constant power load for cryogenic cooling and vacuum pumping (P_{fixed})

$$\eta_{driver}(E, V_f, \omega) = \frac{E\,\omega}{\frac{E\,\omega}{\eta_{pfn} \langle \eta_p (V_f) \rangle} + P_{fixed}}$$

This equation can then be used in plant system studies to give driver efficiencies as V_f, E, and ω are varied.

Our base driver uses: $\eta_{pfn} = 0.5$, E = 5 MJ, ω = 4.6 Hz, P_{fixed} = 5 MW, V_f = 3.83 GV, and V_i = 3 MV, and has a calculated wall plug efficiency of 28%.

2.4.6 Final Compression and Focus Modeling

For final compression and focus, three interrelated processes must be modeled: beam transport, beam compression (longitudinal focus), and beam transverse focus. Analysis and modeling of these processes is a current field of study and can be quite complex, particularly when space charge is important. Our approach, described in the following three sections, is a compromise between detail and study resources required. The analysis and modeling has been done in sufficient depth to give us confidence that the design concepts can be made to work. For the baseline design (Section 2.4.9), slightly different parameters were used in modeling different parts of the system. Development of a consistent set of parameters by further iteration of the design should be straight forward, and we would not expect it to require significant changes in the design concept.

2.4.6.1 Transport

Important constraints on transport include two-sided illumination of the target, simultaneous arrival at the target for all beam bunches, and beam-to-beam separation in the final

focusing quadrupoles. Section 2.4.9.2 describes the specific transport layout and transport system parameters.

Matching the transport line to the focusing system of the linac is simplified by using a FODO focusing lattice in the transport line which has the same period as the one in the linac. Dipole bending magnets are placed between the quadrupoles to make the bending sections. Precision controls will be required to avoid jitter in the position of the beam at the target.

The depressed tune in a FODO lattice is given approximately by:[2.46]

$$\cos(\sigma) - \cos(\sigma_0) = \frac{2KL^2}{(\bar{a})^2}$$

and the mean edge radius of the beam is given by:

$$(\bar{a})^2 = \frac{2\varepsilon L}{\sin(\sigma)}$$

The symbols used in the above equations are defined in Table 2.20. In the modeling, the simultaneous solution of these two equations provides values for the depressed tune and the mean edge radius of the beam.

Table 2.20. Definition of Terms and Symbols for Beam Radius and Tune equations.

SYMBOL	DESCRIPTION	EXPRESSION
σ	Depressed Tune	Given in 2.4.6.1
σ_o	Lattice Tune	
K	Generalized Perveance	$\frac{2I}{(\beta\gamma)^2[B\rho]}\left(\frac{1}{4\pi\varepsilon_o c^2}\right)$
I	Peak Current per Beam	
$[B\rho]$	Beam Stiffness	$\frac{\beta\gamma A m_p c}{qe}$
A	Ion Mass Number	
q	Ion Charge Number	
L	FODO Lattice Half-Period	
$\bar{a}$	Mean Edge Radius of Beam	Given in 2.4.6.1
ε	Emittance	$\varepsilon_n / \beta\gamma$
ε_n	Normalized Emittance	

2.4.6.2 Compression.

The pulse length is compressed by imparting a velocity tilt to the beam with a series of induction modules. The induction modules apply a linearly varying voltage pulse to the beam so that the head of the beam pulse is decelerated and the tail is accelerated. The tilting of the longitudinal phase space ellipse is illustrated in Fig. 2.35, which shows $\Delta p/p$ on the vertical axis and the bunch longitudinal half-width, a_z, on the horizontal axis. In the subsequent drift section the ellipse rotates until it comes to an upright position, and the bunch length is at a minimum. During the final stages of compression, the space charge forces become large and remove nearly all of the coherent velocity spread produced by the bunching voltage. Only the incoherent momentum spread remains, as illustrated in the figure. An example of ten-fold bunch compression, produced by compressor induction modules followed by a drift distance, is shown in Fig. 2.36,[2.47] which shows a_z and $\Delta p/p$ as a function of the drift distance, s.

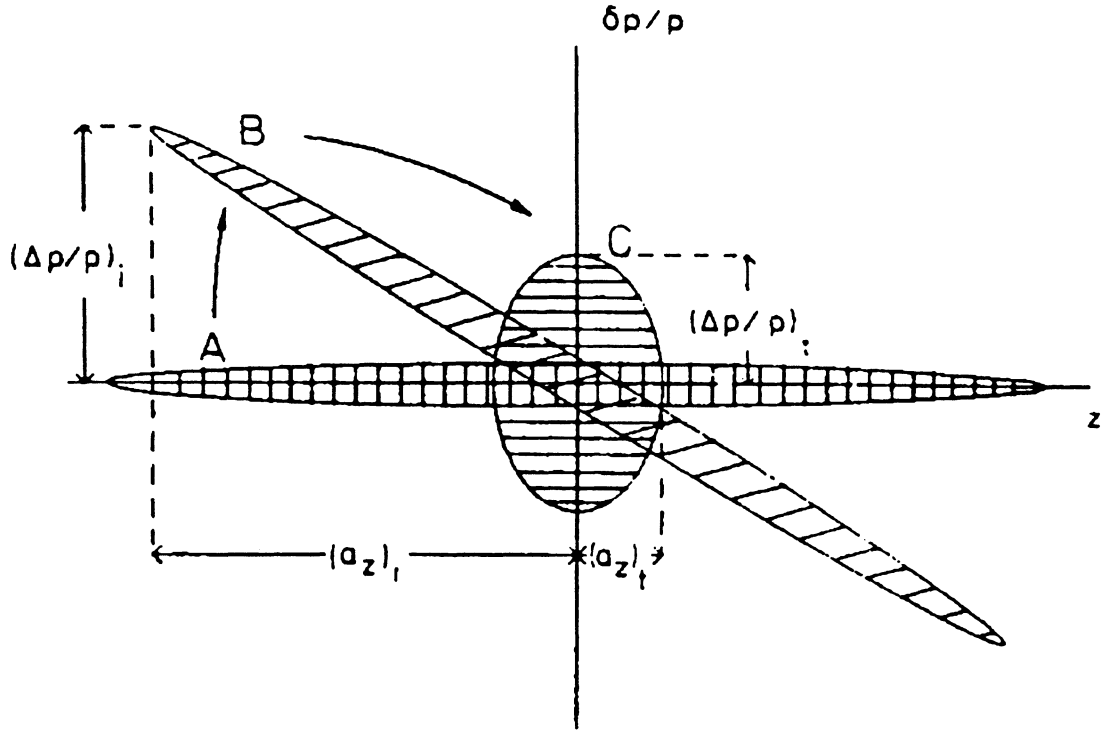

Fig. 2.35. Longitudinal bunch compression. An induction voltage pulse transforms ellipse A into ellipse B, with a large coherent momentum spread $(\Delta p/p)_i$. In a subsequent drift section the rotation is then completed (ellipse C), and $\Delta p/p$ decreases again because of space charge.

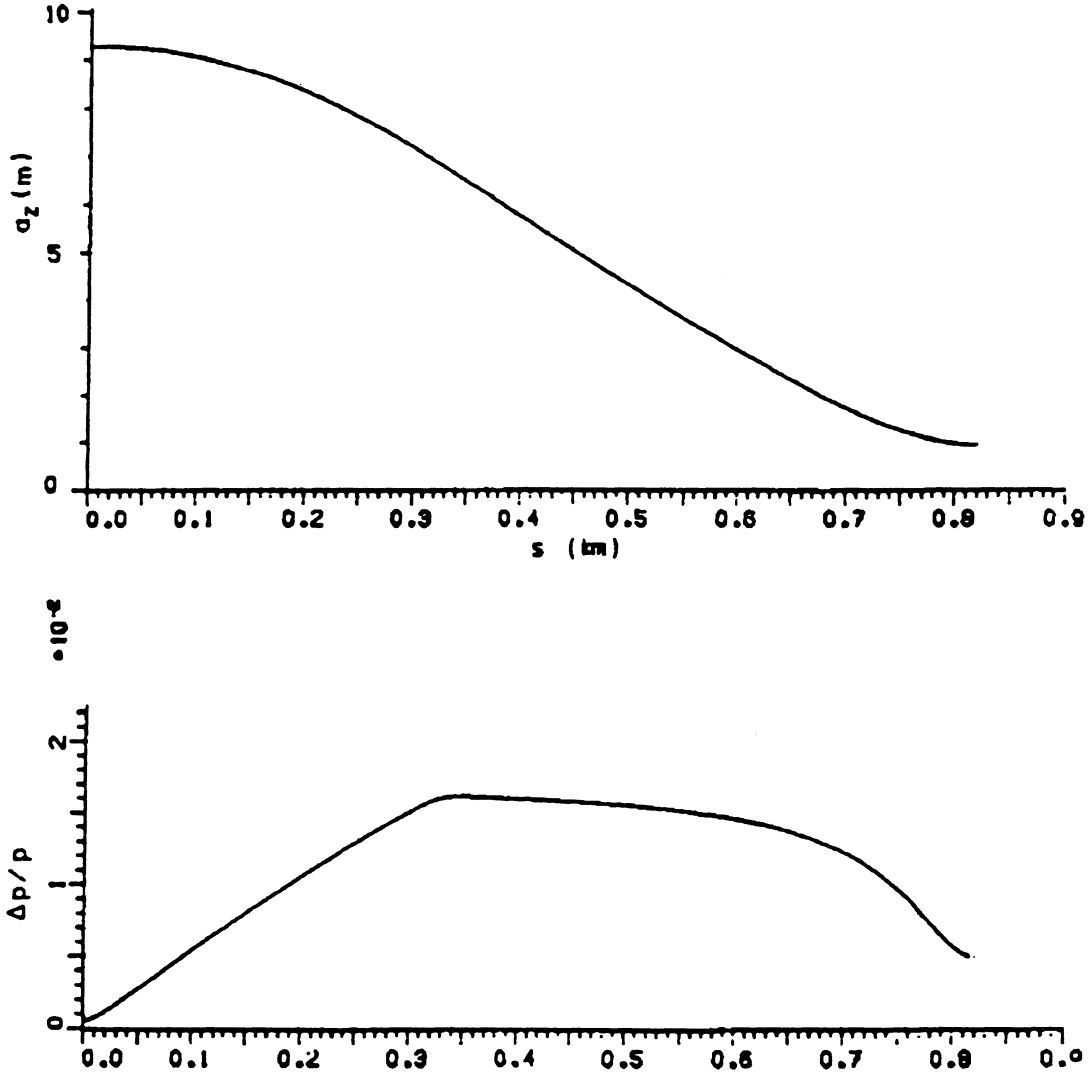

Fig. 2.36. Ten-fold bunch compression produced by 300 meters of compressor induction modules followed by a drift distance. Upper plot: the bunch longitudinal half-width, a_z, as a function of the drift distance, s. Lower plot: momentum spread, $\Delta p/p$, as a function of s.

The velocity tilt required to attain a specified compression is obtained from the equation:[2.48]

$$\text{compression ratio} = \frac{\ell_o}{\ell_f} = 1 + \frac{(\Delta\beta/\beta)^2}{\chi}$$

where ℓ_o is the initial bunch length, ℓ_f is the final compressed bunch length and χ is a dimensionless measure of space charge:

$$\chi = \frac{8\,e}{E_b}\,\frac{g\,\lambda_o}{4\,\pi\,\varepsilon_o}$$

where E_b is the kinetic energy, λ_o is the line charge density at the output of the accelerator, and g is a beam/beam tube geometry factor (which we estimate to be about 1.2 for our system).

The drift distance in a straight transport segment required to remove the tilt and compress the beam is given by:

$$s = \frac{\ell_0 - \ell_f}{\left(\frac{\Delta\beta}{\beta}\right)}$$

Although this equation doesn't apply near the end of the compression where the space charge forces are large, the total drift distance required to remove the tilt and obtain the minimum bunch width can be estimated by setting $\ell_f = 0$.

During compression, the peak beam current increases as the inverse of the bunch length, so the beam perveance K increases (see Table 2.20), and the radius of the beam increases according to the relationships for $\bar{a}$ and σ given earlier. System cost, transport magnet size, and final focus design difficulty all increase with beam size, so the half period of the focusing lattice is decreased gradually during compression to reduce beam radius growth.

2.4.6.3 Final Focus.

Focusing the beams onto the target requires the envelope of each beam to be converging with a half angle of ~ 10-30 mrad at the entrance to the reactor vessel. The simplest lens for making the convergent beam is a quadrupole doublet. At least two additional quadrupoles are

needed to match the beam going into the doublet with the beam emerging from the transport line. Our design for the resulting telescope is described in Section 2.4.9.2.

The upstream telescope quadrupoles are arranged to keep the beam from converging to a small waist within the telescope, in order to reduce the effect of space charge. However, the beam is small enough that our design would have to be modified to take more accurate space charge design calculations into account, and it may be advantageous to add more quadrupoles to the telescope. A final design would have to take into account chromatic corrections and also geometrical aberrations in the large diameter quadrupole lenses. The chromatic effects are minimized by designing the beam compression so that the coherent velocity tilt is a minimum in the center of the final focus system.

Space charge becomes very important as the beam converges to the very small size at the target. This problem is treated in Section 2.4.7.

2.4.7 Reactor Chamber Transport

2.4.7.1 Space Charge

Modeling. A traditional model for beam propagation in the reactor chamber is space charge neutralization (SCN),[2.49] wherein the beam envelope is calculated after specifying that an arbitrary fraction of the beam space charge has been neutralized. We have chosen an alternative model, auto-neutralization (AN),[2.50,2.51] wherein the beam envelope is determined by an auto-neutralizing cloud of hot electrons. By removing the subjective choice of the space charge neutralization fraction, the AN approach provides a higher degree of credibility and at the same time provides physics substance for parameter studies and design choices.

In the AN process, a plasma cloud or other electron source is put in contact with the individual beam bunches near the entrance to the reactor chamber. When the ion bunch separates from the electron source, it has captured an equal number of electrons, so it is macroscopically 100% space charge neutralized. With the traditional SCN modeling, this would mean a zero space charge contribution to the beam spot size. With the more realistic AN modeling, plasma effects within the bunch lead to defocusing of the beam.

Our analysis of AN begins with the trace equation for an ion on the beam envelope

$$\frac{d^2R}{dz^2} = \frac{q E_r(R)}{\gamma m_i \beta^2 c^2}$$

where R is the radial coordinate, z is the position along the beam axis, q is the ion charge state and m_i is the ion mass. $E_r(R)$ is the envelope defocusing electric field and is calculated from the Lemons formula[2.12]

$$E_r(R) = \frac{I_b}{\pi \varepsilon_o \beta c R} K_1\left[\frac{R}{\sqrt{2}\lambda_d}\right] I_1\left[\frac{R}{\sqrt{2}\lambda_d}\right]$$

where I_b is beam current per bunch, K_1 and I_1 are modified Bessel functions of the first and second kind, and λ_d is the electron Debye length

$$\lambda_d = \sqrt{\frac{kT_\perp \varepsilon_o}{e^2 n_e}}$$

where n_e is the bundle electron density and $T_\perp$ is the perpendicular electron temperature.

$T_\perp$ is determined as follows. With the ion bunch in thermal isolation, the electrons are assumed to have an isotropic Maxwell distribution with a temperature taken from previous analysis[2.13] as $T_e = 0.4(m_e/m_i)T_i$, where m_e is the electron mass and T_i is the directed kinetic energy of the beam ions. As the beam bunch converges to the target, the radial electron temperature increases due to radial spatial compression. Because of the high number of electron-boundary collisions during the transport time, electron energy sharing in all three dimensions is assumed. Due to a high axial electron thermal conductivity, the electron temperature is assumed to be approximately constant throughout the bunch at any given time, so the electron compression can be characterized by an average bunch radius, and the perpendicular electron temperature is

given by

$$T_\perp \approx \frac{2}{3} T_e = 0.27 \frac{m_e}{m_i} T_i$$

The defocusing process is terminated upon contact with the target, at which time hot electrons are rapidly replaced by cold electrons, canceling space-charge fields.

The one-dimensional analysis represented by the last four equations yields a beam halo radius but does not provide information on the beam density profile. In applying the analysis, we use the predicted beam halo radius at the target to represent the rms space charge contribution, r_{sc}, to the total beam spot size, r_{total}, thus implicitly assuming the beam density profile is Gaussian.

Figure 2.37a compares two beam envelopes resulting from the AN modeling, and Fig. 2.37b expands the final 1 meter of the representative 5 meter focus. The dotted curve of each figure illustrates a ballistic focus, which is the type of solution described in previous analyses. The solid curve shows a waist focus solution, analogous to the waist solutions of SCN modeling. To achieve the waist solution, the focusing half-angle θ has been increased from the ballistic value of 15 mrad to 16.5 mrad. For this representative case, the additional compression of the waist focus allowed more than 5 times as much ion current to be carried while still achieving the indicated 3 mm envelope spot size.

Because AN waist solutions have not been previously investigated, two concerns regarding their validity were addressed. First, λ_d should be much smaller than the envelope radius over most of the propagation distance so that the electrons provide good shielding of the beam core.[2.13] Although this constraint was found, in general, to be satisfied in AN ballistic solutions, beam compression is much higher for the waist solutions, so the n_e and $T_\perp$ to be used in the equation for the Debye length achieve much higher values. Figure 2.38 compares λ_d with the envelope radius for typical final focus parameters. For these representative parameters, the condition that the Debye length be much smaller than the envelope radius over most of the propagation distance is easily satisfied. For the AN waist solutions in general, we find the small-λ_d-constraint is violated only when r_{sc}^2 is small fraction of r_{total}^2, and in these cases any resulting error would be small.

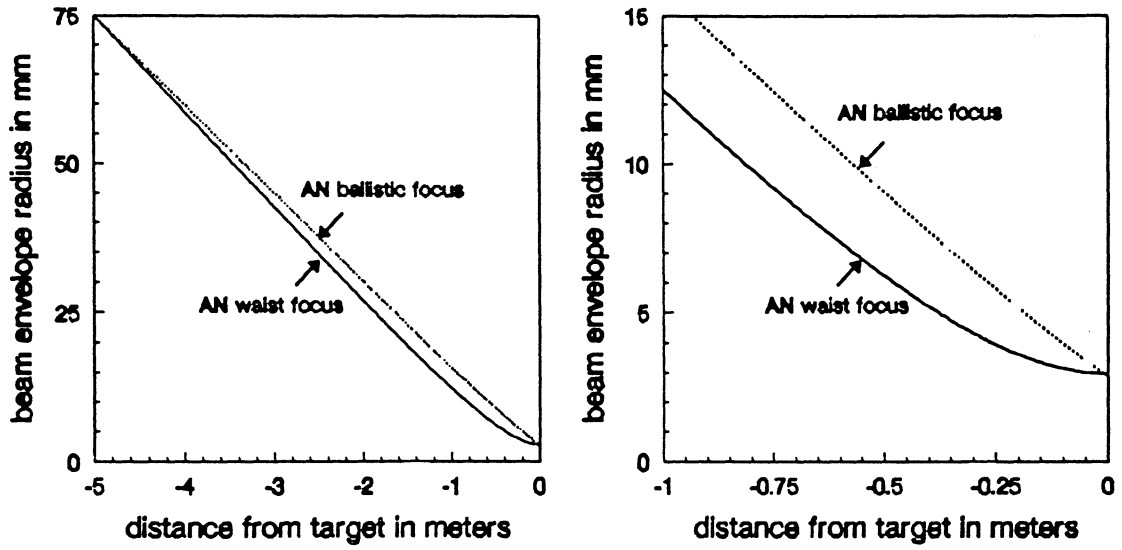

(a) View of Total Focal Length (b) Detail

Fig. 2.37. Beam envelopes from auto-neutralization model.

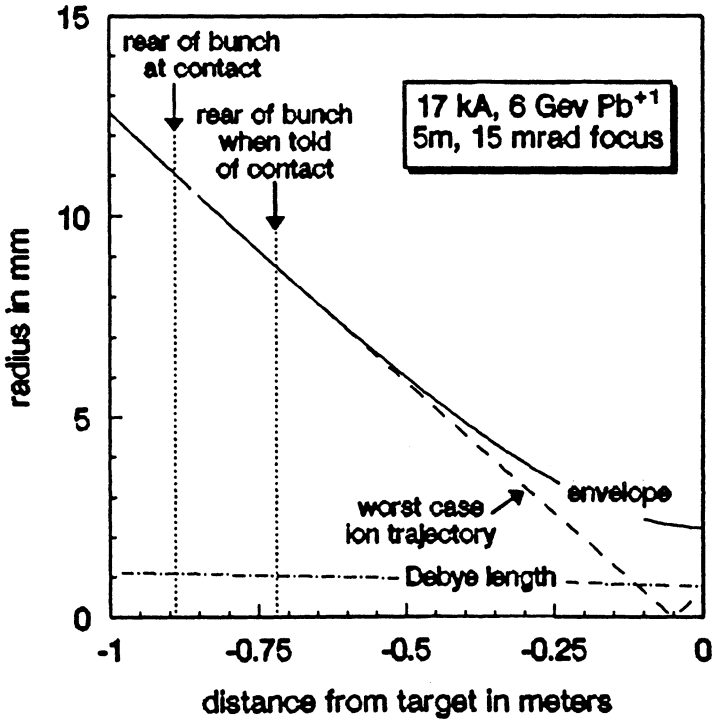

Fig. 2.38. Beam envelope, Debye length, and worst-case trajectory.

The second concern is whether all ions in the bunch will actually hit the target in the case of a waist focus. In the AN model, cold electrons cancel the space charge fields when the head of the beam contacts the target. Without space charge fields, ions proceed on ballistic trajectories. If we assume that the beam envelope trace represents the shape of the beam bunch, the AN modeling can be used to determine whether the worst-case trajectory (trajectory of the ion most likely to miss the target) intercepts the target.

This is illustrated in Fig. 2.38, which shows, as the left-most dotted vertical line, the position of the rear of the beam bunch at the instant the nose reaches the target. By inspection, it can be seen that the ions at the outside rear of the bunch are most likely to miss the target; with sufficient d^2R/dz^2 on the envelope, these ions might cross the axis and miss the target. Note, however, that cancellation of the electric fields within the bunch cannot occur throughout the bunch instantaneously, but rather will be communicated from the target at a velocity no faster than the velocity of light, c. Assuming a communication speed, v_{comm}, is equal to c, the right dotted vertical line shows the position of the rear of the bunch when the ion trajectories become ballistic. The dashed line is the extrapolation of the worst-case trajectory (crossing the axis is shown as a reflection), and for the representative parameters, these trajectories easily strike the target.

From Fig. 2.38, these worst-case trajectories become more favorable as v_{comm} is decreased from c. A good guess for v_{comm} might be the final electron thermal velocity, $\approx$ c/2. However, even when using the conservative value v_{comm} = c, we find that worst case trajectories begin to miss the target only when r_{sc}^2 is small fraction of r_{total}^2. Again, as with the small-λ_d-constraint, any resulting error in these cases would be small.

Parametric Algorithm. A fast and reasonably accurate algorithm for predicting r_{sc} as a function of principal driver parameters (e.g., kinetic energy E_b (= q V_f), focal length L_f, θ, q, and m_i) was needed to support the PC-based accelerator optimization code (see Sections 2.4.4 and 2.4.8). The AN analysis described in the previous section does not lead to closed-form equations, and the primary analysis was done with an large fortran code residing on a VAX.

The PC algorithm was created as follows: Because the initial (point of neutralization) electron Debye length, λ_{di}, is the key parameter which determines many of the dependencies on beam parameters[2.12] (in particular, λ_{di} carries the current-per-beam information), the equation for

λ_d was recast in terms of the driver parameters. The initial electron density, n_e, is equal to q times the initial ion density, n_i. n_i is calculated as the total ions in a bunch, $I_b t_b/qe$, divided by the bunch volume, $\pi \bar{R}^2 \beta L_b$, where t_b is the pulse width, $\bar{R}$ is a mean radius for the initial bunch volume, and $L_b = \beta c t_b$ is the bunch length. Combining gives:

$$n_e = q n_i = \frac{(I_b/e)}{\pi \bar{R}^2 \beta c}$$

In the Fortran code, the bunch volume is defined by the details of the beam envelope. A good approximation to the code value of $\bar{R}$ is given by assuming the bunch is a truncated cone converging at the geometric focusing half-angle, θ (as opposed to the slightly larger focusing angle actually used to provide the waist). The initial state of the bunch becomes fixed at the time when the trailing edge of the bunch loses contact with the electron source. This gives $\bar{R} = \theta \, (L_{inj} - L_b / 2)$, where L_{inj} is the distance from the target to the point of electron injection.

With these substitutions, the input electron Debye length can be calculated in terms of beam properties and focus geometry:

$$\lambda_{di} \approx 0.516 \, \theta \left(L_{inj} - \frac{L_b}{2} \right) \sqrt{\left(\frac{m_e}{m_i} \right) \frac{E_b \, \varepsilon_o \, \pi \, \beta \, c}{e \, I_b}}$$

Values calculated for the Debye length from the above equation are typically within a few percent of the values calculated by the fortran code.

With the simplified expression for λ_{di} in hand, the sequence for developing the $r_{sc}(\lambda_{di}, E_b, L_{inj}, \theta, q, m_i)$ algorithm was:

1. Define a base point parameter set.
2. Assume separability such that the fit will be:

$$r_{sc}(\lambda_{di}, E_b, L_{inj}, \theta, q, m_i) = C \, W_1(\lambda_{di}) \, W_2(E_b) \, W_3(L_{inj}) \, W_4(\theta) \, W_5(q) \, W_6(m_i)$$

As shown earlier, λ_{di} is a function of the parameters E_b, L_{inj}, θ, q and m_i, so

separability here means that the basic λ_{di} dependence, with these parameters fixed, is separated from additional dependencies observed when these parameters are varied individually.

3. Vary the current per beam at the base point in order to examine the code-predicted waist-size-vs-λ_{di} behavior with other parameters fixed; invent an algorithm, $W_1(\lambda_{di})$, to fit the behavior.
4. Vary E_b only, compare the code-predicted waist with $W_1(\lambda_d)$, and invent the fit $W_2(E_b)$ to provide the additional E_b dependence observed.
5. Repeat step 4 for L_{inj}, θ, q and m_i.

The algorithm resulting from this ad-hoc procedure, when using a base point of E_b = 5 GeV, L_{inj} = 5 m, θ = 30 mrad, q = +1, m_i = 207 (Pb), I_b = 76.8 kA and t_b = 11.1 nsec, is summarized in Table 2.21. The derived λ_{di} is 1.27 mm. Each of the fit factors W_n have been normalized to be 1.00 at the base point, so the coefficient C is equivalent to r_{sc} at the base point, 2.86 mm.

The code-predicted θ-dependence begins to change dramatically below about 13 mrad, as does the code-predicted mass dependence below 108 AMU (Ag). No attempt was made to fit this behavior, so algorithm errors at these extremes become larger, as shown in the table. If these regimes were of interest, it is likely that shifting of the base point towards these values would provide better agreement.

Our baseline driver parameters, which were selected after the algorithm was developed, turned out to differ substantially from the derivation base point in several respects: 3.83 GeV Xe^{+1} was chosen rather than 5 GeV Pb^{+1}, and the choice of 12 beams resulted in λ_{di} = 3.09 mm rather than 1.27 mm. (Note that the debye length decreases from this initial value as the beam approaches the target. For the baseline driver parameters, the debye length is always less than the beam envelope radius.) As indicated in the table, individually these changes do not result in large algorithm error. However, the combination was observed to result in a systematic error of 23%. As a quick fix, the constant C was reduced to 2.22 mm for use with the baseline design. For further work, a re-derivation with a base point equal to, or closer to, the baseline parameters is recommended.

Table 2.21. Description and Evaluation of the Fit:

$$r_{sc}(mm) = 2.86\ W_1(\lambda_{di})W_2(E_b)W_3(L_{inj})W_4(\theta)W_5(q)W_6(m_i)$$

PARAM (UNITS)	ALGORITHM W_n(PARAM)	BASE CASE VALUE	RANGE EXAMINED VALUES	RANGE EXAMINED ERROR
λ_{di}(mm)	$55.9(\lambda_{di}+2.2)^{-3.228}$	1.27 mm	0.80 mm 3.0 mm	-1.1% +0.2%
E_b(GeV)	$1.20-6.96\times10^{-2}E_b+8.69\times10^{-3}E_b^2$ $-5.35\times10^{-4}E_b^3$	5 GeV	2.44 GeV 14.9 GeV	+1.4% +4.5%
L_{inj}(m)	$0.398-0.233L_{inj}+0.131L_{inj}^2$ $-2.26\times10^{-2}L_{inj}^3+2.11\times10^{-3}L_{inj}^4$	5 m	3 m 10 m	-1.0% -0.1%
θ(mrad)	$1.66-4.372\times10^{-2}\theta+9.72\times10^{-4}\theta^2$ $-8.34\times10^{-6}\theta^3$	30 mrad	12.5 mrad 13.0 mrad 50 mrad	+27% +1.8% -0.1%
q(e)	$0.371+9.59\times10^{-2}q+0.533q^2$	1	1 7	0 +0.2%
m_i(AMU)	$2.47-7.07\times10^{-3}m_i$	207.2(Pb)	95.9 (Mo) 108.(Ag) 238.(U)	+53% +0.1% -9.7%

2.4.7.2 Beam Spot Size

The beam spot size, r_s, has contributions from effects in addition to space charge. We estimate r_s as the rms total of the contributions from AN (space charge), emittance, dispersion, and jitter/alignment:

$$r_s^2 = r_{sc}^2 + r_\varepsilon^2 + r_{\Delta p}^2 + r_{jitter}^2$$

By doing rms combining, we have implicitly assumed Gaussian beam profiles. The emittance spot size, r_ε is calculated as $\varepsilon_n / (\beta\gamma\theta)$, where ε_n is the normalized emittance. The

dispersion spot size, $r_{\Delta p}$, is calculated[2.52] as $8 L_f \theta \Delta p/p$, where $\Delta p/p$ is the incoherent beam momentum spread.

Figures 2.39 and 2.40 compare typical AN contributions (dashed) with typical contributions (dotted) from emittance, dispersion and jitter/alignment. Also shown on each of the figures is r_s (solid). An ε_n of 1 x 10^{-5} meter-radians was used for r_ε, and a $\Delta p/p$ of 1 x 10^{-3} was used for $r_{\Delta p}$. The jitter/alignment contribution was arbitrarily assumed to be 180 μrad. Figure 2.39 displays the spot contributions as a function of the beam kinetic energy, and shows, for these representative parameters, the AN component to be dominant at low energy and the emittance component to be dominant at high energy. Figure 2.40 uses focusing angle as a variable, and shows AN and emittance both contribute at small angles, while dispersion dominates at large angles. For the θ = 15 mrad used in the example, dispersion is not important. As a function of θ, a weak minimum in spot size is observed at 30 mrad. This minimum becomes more pronounced, and the optimum angle decreases, as the momentum spread increases from 1 x 10^{-3}.

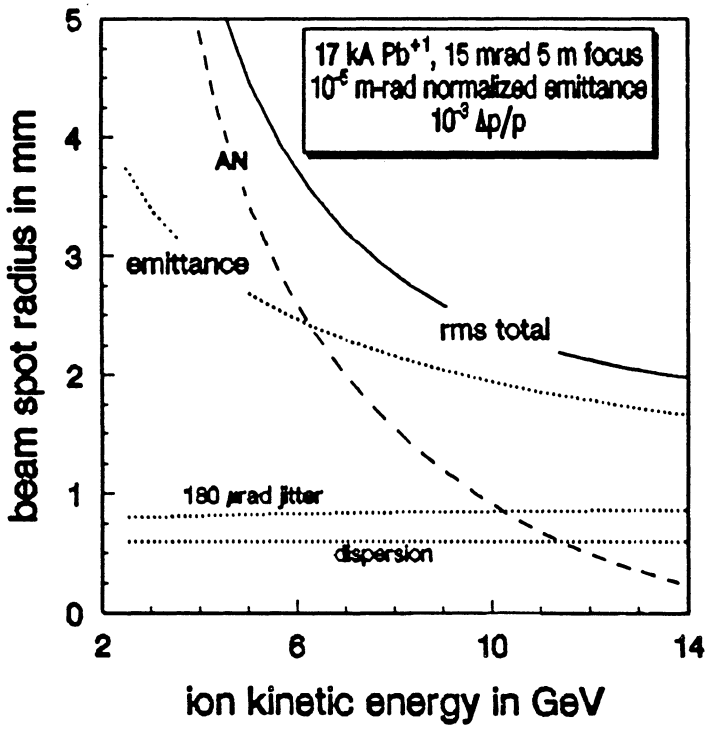

Fig. 2.39. Spot size composition vs. kinetic energy.

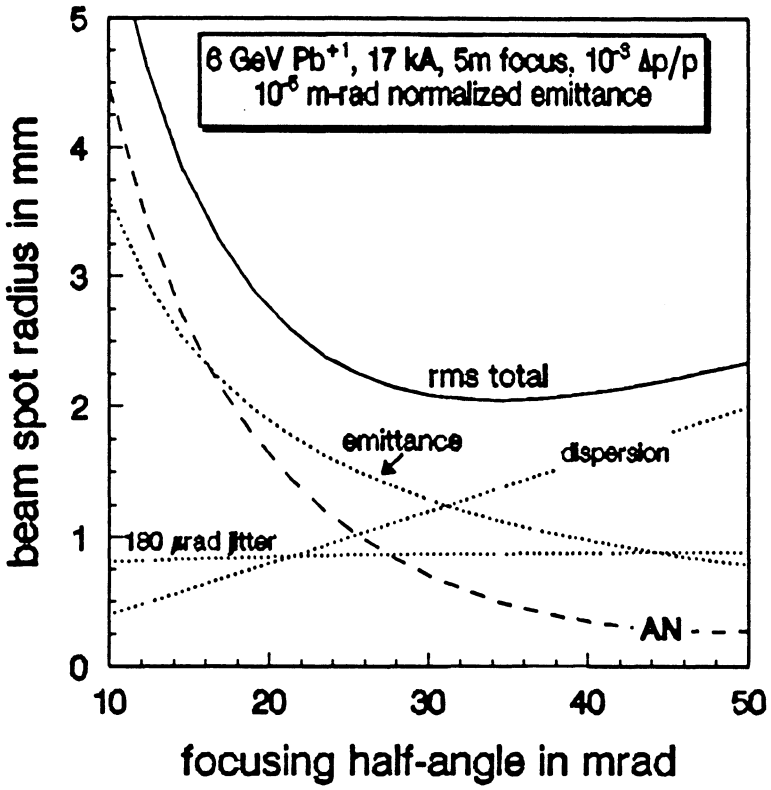

Fig. 2.40. Spot size composition vs. focusing angle.

Spot size predictions with AN modeling can be quite sensitive to the distance from the target at which the auto-neutralizing electrons are supplied. This is illustrated in Fig. 2.41, where it is assumed that the auto-neutralizing electrons are supplied at the beginning of the focus ($L_f = L_{inj}$). The figure shows that at constant θ, r_{sc} increases strongly with L_f (= L_{inj}), as does r_s for our example parameters wherein r_{sc} contributes significantly to r_s.

This dependence on length, which is much stronger than is seen with SCN modeling, occurs because more length results in more bunch compression, leading to higher electron temperatures and higher defocusing electric fields. So with the AN modeling, final focus performance improves significantly with decreasing distance between the point of electron injection and the target. In our baseline design, this is reflected in a relatively small chamber radius, allowing a smaller electron injection length, and in the choice of a sufficient number of paralleled beams such that the r_{sc} contribution to r_s is small, and the resulting r_s dependence on L_{inj} is not as pronounced.

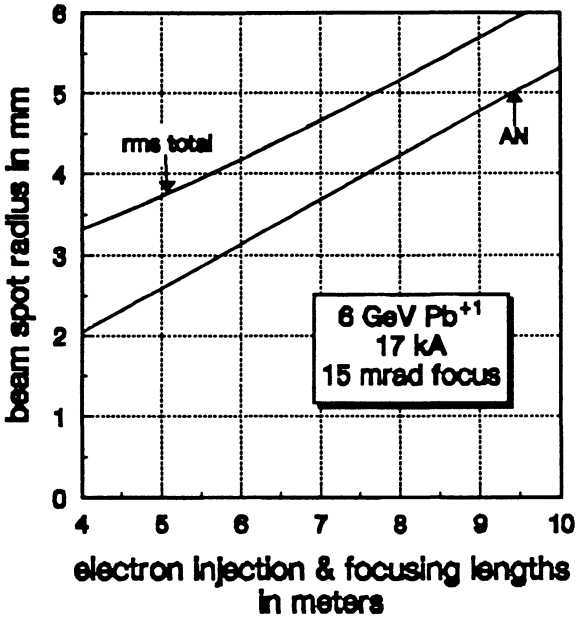

Fig. 2.41. Spot size vs. distance from electron injection.

2.4.7.3 Stripping

In contrast to SCN modeling, the AN model allows for chamber stripping without ambiguity. The essential effect of stripping is to add electrons and ion charge. For the < 100% fractional neutralization of the SCN model, this would change the neutralization fraction, thereby violating the model's basic assumption. Stripping is incorporated into the AN differential equation by incrementing the bunch electron density, incrementing the bunch average ion charge state, and diluting the bunch electron temperature for each stripping event. Stripping cross sections were estimated using the following parametric fit[2.53] to published calculations:[2.54]

$$\sigma_s \approx \frac{2.45\times10^{-18}\,\mathrm{cm}^2}{\beta^2}\left(\frac{Z_{gas}}{3}\right)\left(\frac{Z_i}{92}\right)\exp(-0.063\,q)$$

where Z_{gas} is the gas atomic number (x 2 for diatomic gases) and Z_i is the beam atomic number. The coefficients were picked to match U on Li data.

Typical stripping assessments are displayed in Fig. 2.42, which shows r_{spot} as a function of the cumulative fractional stripping attained when the beam bunch reaches the target. The solid

curves are for fixed focusing lengths L_f of 4, 5 and 6 meters, while the dotted curves are for the constant Li, Be, F or Pb vapor densities indicated. As inferred by Fig. 2.42, we find that stripping of tens-of-percent is not disastrous, and can be accommodated in system trades. Table 2.22 gives calculated densities along with the self-consistent vapor pressures and vapor temperatures which yield 20% stripping with our example parameters (i.e., 10 GeV Pb ions with L_f = 5 m).

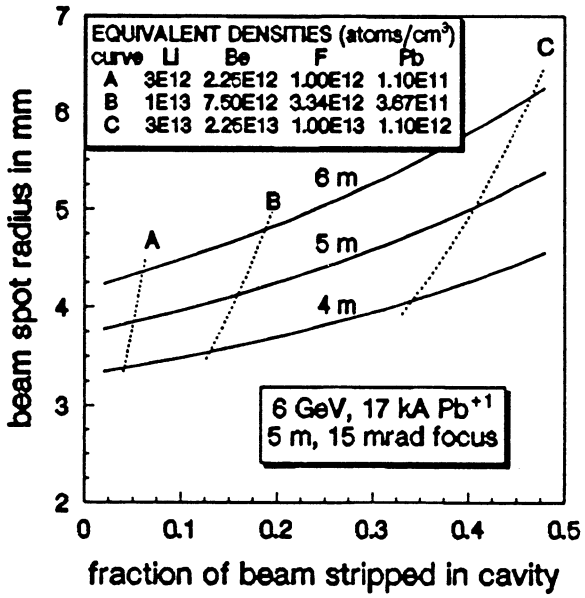

Fig. 2.42. Impact of beam stripping in reactor chamber.

Table 2.22. Vapor Densities, Pressures and Temperatures for 20% Stripping

VAPOR	DENSITY	PRESSURE	TEMPERATURE
Lithium	1.3×10^{13} cm^{-3}	9.9×10^{-4} torr	740 K
Lead	4.7×10^{11} cm^{-3}	4.0×10^{-5} torr	805 K
Flibe	2.5×10^{12} cm^{-3}	2.2×10^{-4} torr	824 K

2.4.8 Parametric Studies

2.4.8.1 Description of Parametric Studies

Parametric studies were done to choose a driver design with low cost and beam parameters which produce a high target gain. Scaling of target performance and driver cost was done for several driver parameters including:

- driver energy (E),
- number of ion beams (N),
- type of superconductor used in focusing magnets (NbTi or Nb_3Sn),
- maximum magnetic field allowed at the windings (B_{max}),
- axial packing fraction for the quadrupole fields (η),
- ion mass (A), and
- ion charge state (q).

Driver Assumptions Modeled. The goal of this study was to find the most affordable driver that does not require any aggressive design assumptions. Driver costs may be lowered if beam combination, beam separation, and recirculation can be used, but it is possible that some (or all) of these options will degrade or destroy beam quality and target performance. Beam combination and recirculation degrade target performance by increasing the beams emittance (crudely described as the product of the beam's radius and its angular divergence). Beam separation can theoretically produce two beams with lower emittance than the parent beam, but introduces other uncertainties. Beam separation requires complicated separation magnet designs which introduce the potential for ion loss or beam quality degradation, and increasing the number of beams at the reactor complicates the design for the final focussing systems and the reactor/driver interface.

For each set of driver parameters, we design the shortest possible driver and examine its cost. As discussed earlier in this chapter, we minimize the required driver voltage (and therefor the required length) by using the highest beam currents allowed for a given set of driver focusing parameters.

The Choice of a Base Driver Design. The base driver was chosen by examining the target gain and a driver cost contributions (a subset of the total direct costs) of 5 MJ drivers using a wide variety of driver parameters. The driver cost contributions used were the costs of

the quadrupole arrays and the inductor metglas cores. Limiting the cost figure of merit to the sum of these two elements was justified because the costs of other expensive components (support structures, the pulse forming network, the cryogenic cooling system, etc.) scale with core or quadrupole array requirements.

A true multivariable optimization was not done. While some design variables were optimized (e.g., the focusing angle was selected to give the minimum spot size for each design considered), other variable choices were made by picking a point from a parametric curve. A precise minimization of gain per unit cost was not done; rather, a sensible choice near the point of diminishing return is made for each parameter (usually the "knee" of the curve of target gain vs. parameter value). By adjusting the driver design one parameter at a time and then re-examining the choices of the other parameters (ion mass, number of beams, maximum magnet field at quadrupole windings, linear occupancy factor for the quadrupole fields, etc.), the cost and performance of the driver can be greatly improved.

The entire parametric search is not reproduced here, but several representative variations and chosen parameters are shown. The total costs for our base driver and plant are described in Chapter 8.

2.4.8.2 Cost and Gain Scaling

Parametric sensitivity studies were done for 5 MJ drivers. For all driver parameters, except the number of beams used, smooth curves can be created for the dependence of the driver cost and predicted target gain on the parameter value. Because the relationship between quadrupole magnet dimensions and the array radius is different for each choice for the number of beams, drivers were chosen for several possible values of N and these drivers were then compared. Five MJ driver designs with 4, 12, and 24 beams were compared. These values of N were chosen because they provide the highest packing fractions when the beams are stacked (with 4-fold symmetry to provide return paths for the magnetic fields) to fill a circle.

The axial packing fraction of quadrupole fields, η, is the fraction of the driver length occupied by the quadrupole fields. For a constant beam radius, the axial packing fractions for the entire driver will be limited by the maximum allowable initial packing fraction, η_i. Because greater focusing along the beam lines allows for greater beam currents larger values of η_i will give the shorter drivers. As shown in Figure 2.43, there can be a range of packing fractions with

comparable combined costs, but several cost which are not included (e.g., power distribution and tunnel construction) favor shorter systems.

When analyzing the effect of other driver variables on driver performance and cost, we fix the maximum field at the quadrupole superconductors at 10 Tesla. For drivers using singly charged ions (q = 1), we compared systems using the highest credible initial packing fraction which was taken as $\eta_i = 0.8$. For higher charge state ions (q = 2 or 3), high packing fraction were not as important and $\eta_i = 0.5$ was chosen.

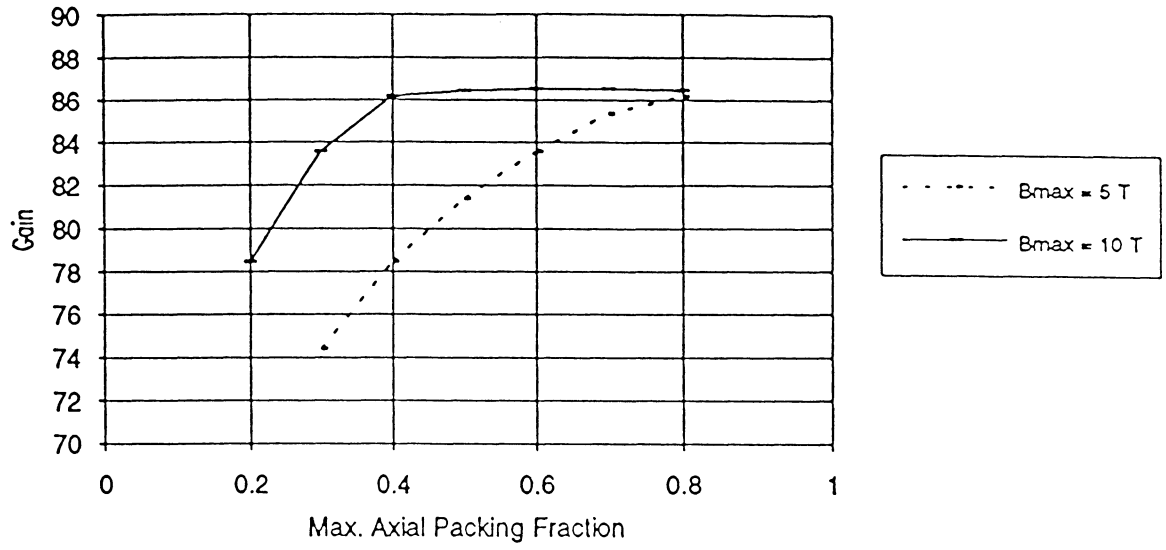

Fig. 2.43a. Gain vs. maximum quad packing fraction.

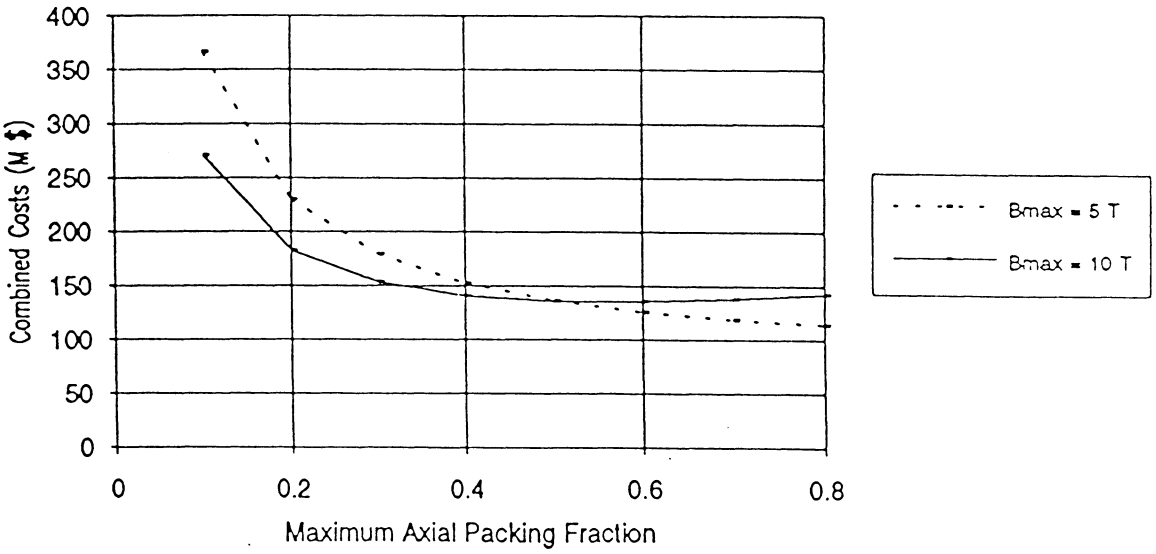

Fig. 2.43b. Combined costs vs. maximum quad packing fraction.

Figure 2.44a shows the achievable target gain for 12 beam 5 MJ drivers as a function of ion mass, A. Each point corresponds to a different driver designed to give the lowest required voltage for the chosen value of A. For a 12 beam driver, gain increases for drivers designed to use higher A and decreases for designs using higher values of q. (A driver designed for higher values of q will have a lower voltage, and hence a smaller range, but will have a larger spot size resulting from its higher beam currents.) For drivers using singly charge ions there is little benefit to using values of A higher than 150.

Figure 2.44b shows the combined costs for the same drivers. Although drivers using ions with higher charge states can have lower costs than those using singly charged ions, they also have lower gains. For our base driver, we selected ions with q = 1 and A = 131 (Xe) for a conservative design with costs slightly above those of the least expensive driver.

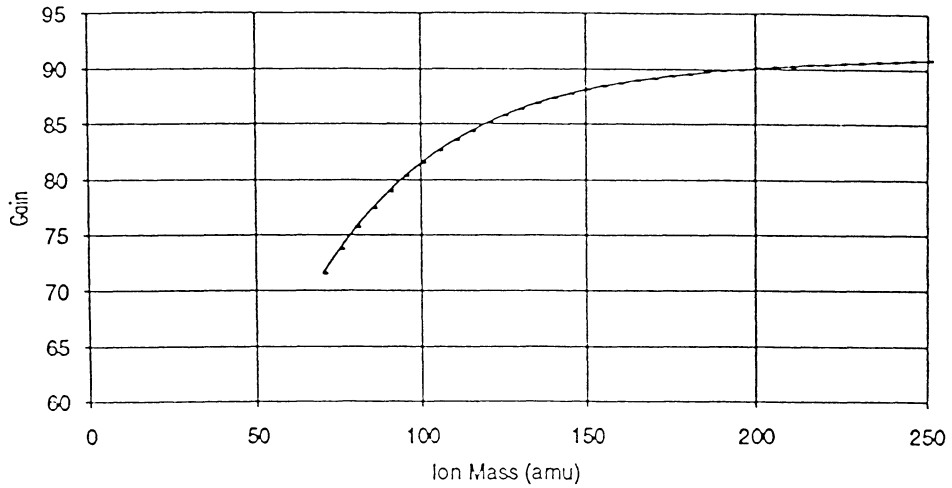

Fig. 2.44a. Gain vs. ion mass for base driver designs.

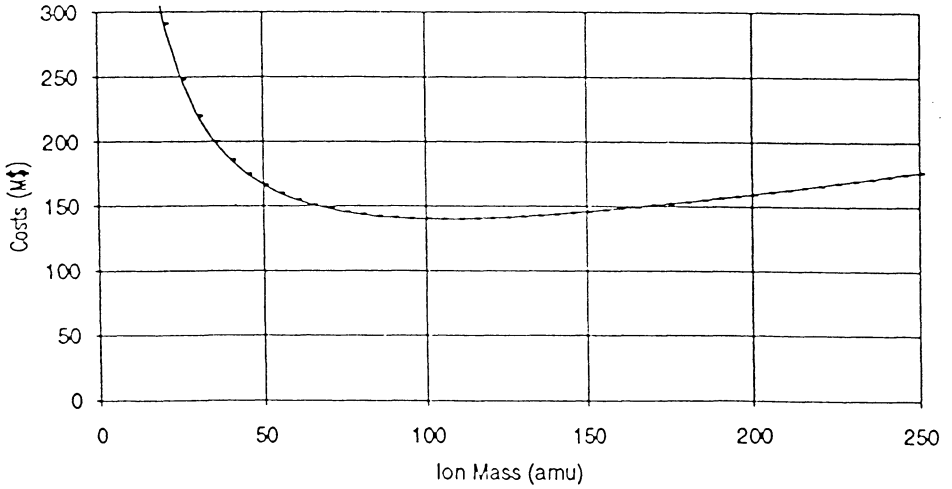

Fig. 2.44b. Combined cost vs. ion mass for base driver designs.

Although cost calculations were only done for a few values of N, the achievable gains were calculated for all possible values of N. (As mentioned earlier, costing depends on array designs which are unique for each value of N. Beam parameters needed for gain calculations, on the other hand, can be found without doing new array designs.) Figure 2.45 shows the dependence of target gain on N for 5 MJ drivers using A=131, η_i = 0.8, and B_{max} = 10 T.

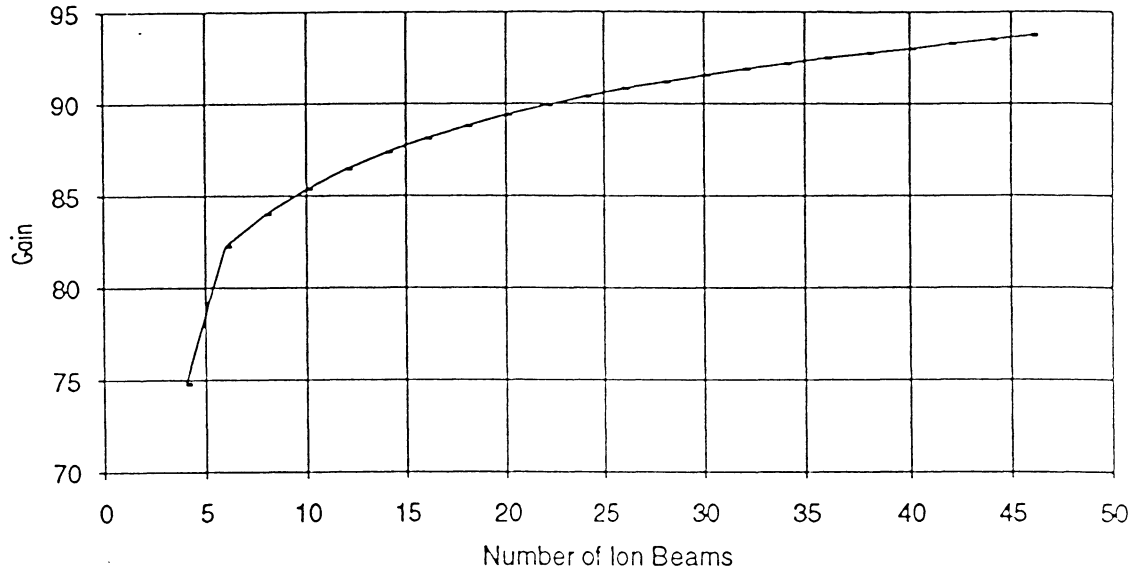

Fig. 2.45. Gain vs. number of beams for base driver designs.

We found that optimized 12 and 24 beam driver designs have similar cost and performance. The 12 beam driver was chosen for the base case because it allows for a simpler reactor interface. In addition, the difference between predicted and actual target performance is likely to be smaller for the 12 beam system. The spot sizes used in the gain calculations are those for a single beam. The physics of beam combination at the target will probably give a net spot size for all beams that will be slightly larger than the single-beam spot size. Degradation of net spot size will probably be worse for the 24 beam driver.

Higher charge state ions require complicated sources and have a higher potential for electron capture, but may have lower cross-sections for electron stripping. Because the cost saving from the use of high charge states are small and come at the expense of target performance, we chose a q = 1 driver as our base design.

Figure 2.46 and Table 2.23 show the cost savings resulting from driver parameter changes.

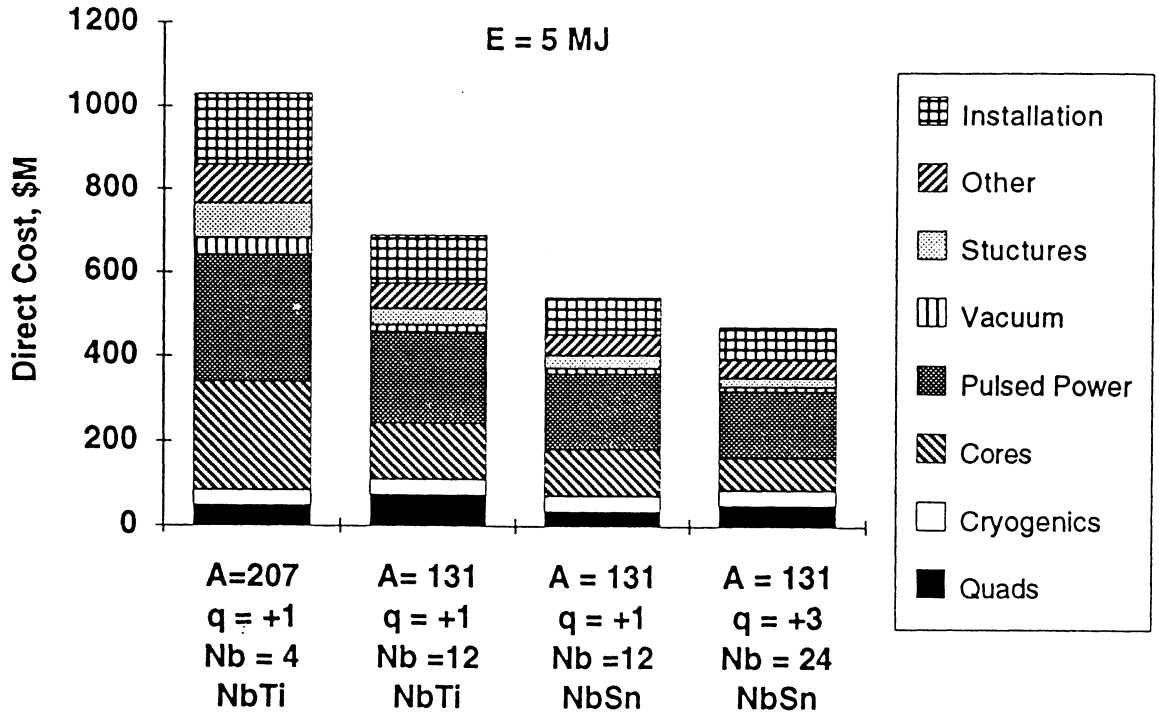

Fig. 2.46. Cost comparison of four possible heavy-ion driver designs.

Table 2.23. Parameters for Four Possible Heavy-Ion Driver Designs

Parameter	A = 207 q = 1 NbTi	A= 131 q = 1 NbTi	A = 131 q = 1 NbSn	A = 131 q = 3 NbSn
Energy, MJ	5	5	5	5
Number of Beams	4	12	12	24
B max at S/C, T	6	6	10	5
Initial Quad Occupancy	0.6	0.8	0.8	0.6
Final Voltage, GV	11.64	4.81	3.83	2.59
Current Per Beam, kA	1.07	0.87	1.09	0.81
Final Pulse Width, ns	100	100	100	100
Accelerator Length, km	13.8	5.8	4.8	3.4
Driver Efficiency, %	16.6	23.3	28.2	31.9
Spot Radius, mm	2.0	2.1	2.3	2.0
Ion Range, g/cm^2	0.15	0.10	0.07	0.18
Gain	80	86.4	86.4	73.8
Yield, MJ	400	430	430	370
Quad Arrays	1284	1202	1978	1741
Total Quads	5136	14424	23736	41784
Total Cores	23387	9446	7643	5001
Total Direct Cost, $B	1.03	0.69	0.54	0.47

2.4.9 Description of the Base 5 MJ Driver Design

2.4.9.1 Base Accelerator Design

The base design for a 5 MJ accelerator was chosen after several parametric variation studies. The optimum value for each driver parameter depends on the chosen value of all the other variables, so an iterative approach was used to set the base parameters. The chosen driver parameters led to a 4.81 km long driver shown in Fig. 2.47. The driver parameters for this base design are shown Table 2.24.

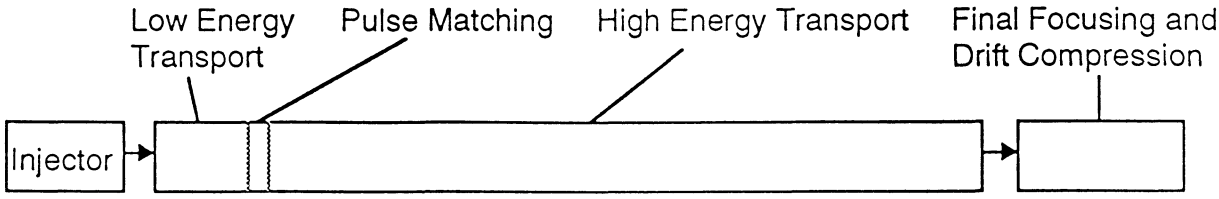

	Injection	Beginning of PM Stage	Beginning of HET Stage	End of Accelerator
X	0 m	359 m	392 m	4.81 km
Φ	12.6 kV/m	0.85 MV/m	0.85 MV/m	0.85 MV/m
V	3 MV	49.7 MV	78.1 MV	3.83 GV
I_b	3.46 A	57.4 A	168 A	1.09 kA
τ	34.1 μs	2.06 μs	703 ns	100 ns
I	71.4 m	17.5 m	7.49 m	7.49 m

Fig. 2.47. Base heavy-ion driver schematic.

Table 2.24. Base Case Heavy-Ion Parameters

Energy, MJ	5	Max. axial Quad. occupancy	0.8
Ion Mass, amu	131		
Charge State	1	Quads:	
Superconductor	NbSn	Number of Arrays	1978
Number of Beams	12	Number of Quads	23736
B max at S/C, T	10	Effective Field Length, cm	18.1
Driver Efficiency, %	28.2	Quad Length, cm	22.6
Beam Voltage		Beam Radius, cm	6.8
Initial, MV	3	Quad Bore, cm	8.9
Final, GV	3.83		
Current per Beam		LET Cores	
Initial, A	3.5	Number	804
Final, kA	1.09	Length, cm	20
Pulse Length		Radial Build, cm	80
Initial, microseconds	34	HET Cores	
Final, nanoseconds	100	Number	6840
Accelerator Length		Length, cm	10
Low Energy, m	359	Radial Build, cm	40
Pulse Compression, m	33		
High Energy, km	4.4	Total Metglass, MT	14.3
Total Length, km	4.8		
Final focus half-angle, mrad	33		
Spot radius, mm	2.3		
Ion Range, g/cm^2	0.07		
Gain	86.4		
Yield, MJ	430		

Once the base driver parameters were chosen, we investigated the effect of changing the chosen driver energy. The models presented in the previous sections were used to calculate driver sizes and cost contributions for drivers using our base driver assumptions at a variety of possible driver energies. Figures 2.48a and 2.48b shows how the target gain and combined costs vary with driver energy for our base driver assumptions.

By combining our base driver model with models for chamber and balance of plant costs, we can determine the effect of driver energy and repetition rate on the cost of electricity and total direct costs of a power plant. As discussed in Chapter 8, the minimum cost of electricity occurs at somewhat lower driver energy, but the savings are less than 5% of the total cost of the base driver design discussed here.

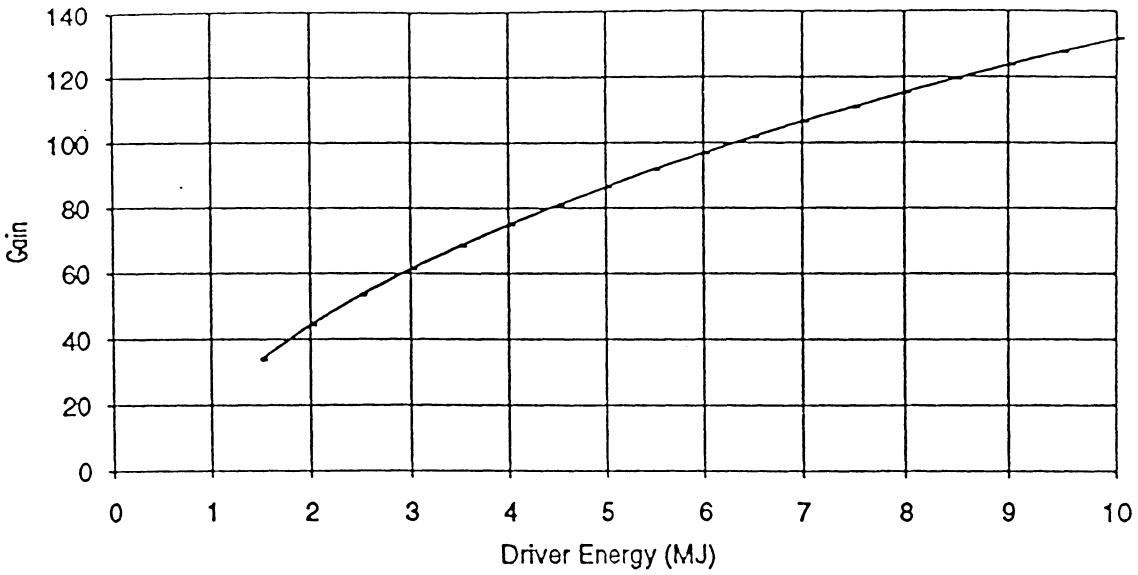

Fig. 2.48a. Gain curve for base driver assumptions.

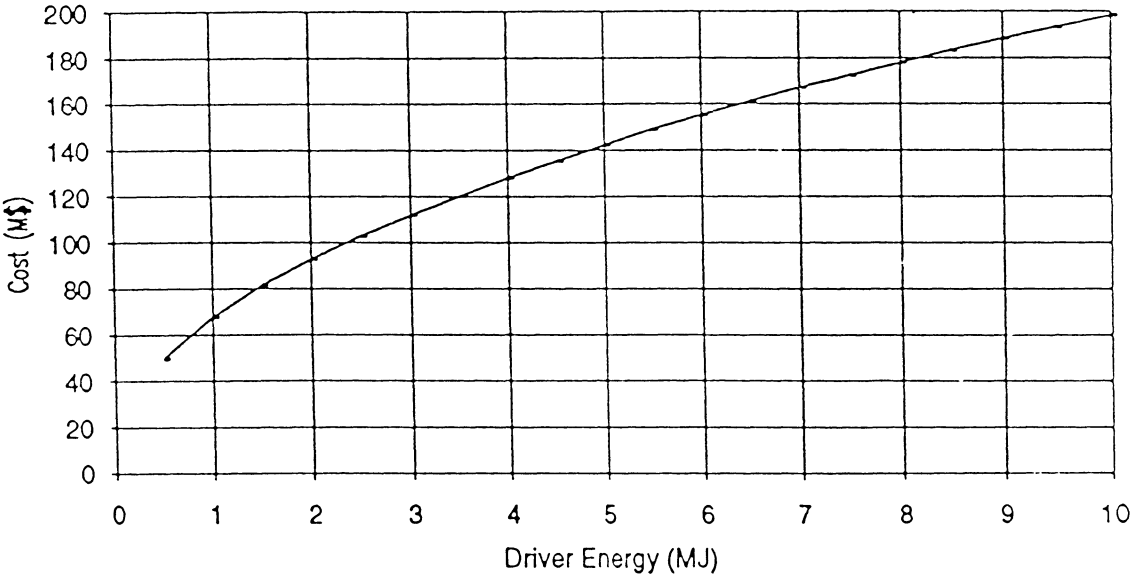

Fig. 2.48b. Cost subtotal for base driver assumptions.

2.4.9.2 Base Final Transport Design

The final compression and focus segment matches the 3.83 GeV Xe^{+1} linac output beam to the parameters specified at the target. Table 2.25 shows key input and output match-up parameters for the final compression and focus. Although there is no specification on pulse shape, we have constrained our design such that each of the individual beam tubes is the same length, and therefore each will deliver its respective beam bunch at the same time. Final gain optimization (see Section 2.4.4.2) resulted in an optimum focusing half angle of 33 mrad. We present here an earlier final transport design predicated on a 24 mrad optimum angle. We were able to design a 33 mrad final focus telescope prior to the end of the contract, but we did not have time to complete the integration of that design into the final drift, compression, and focus calculations. It is clear from this effort that the larger focusing angle stresses the final transport design: it increases the beam bundle size, the focusing quadrupole sizes, and the telescope length, and it decreases the spreader bend radius. We conclude that minimum beam spot size should not be the only criteria for determining the final focus angle.

Table 2.25. Input and Output Parameters for Final Compression and Focus

PARAMETER	INPUT FROM LINAC	SPECIFIED AT TARGET
Number of Beams	12	12
Bundle Geometry	Close-packed Rectilinear	Two 6-beam Hexagonal Rings
Current per Beam	1.09 kA	10.9 kA
Pulse Width	100 nsec	10 nsec
Beam Envelope Radius	6.8 cm	0.23 cm
Normalized Emittance	1×10^{-5} meter-radians	
Momentum Spread	1×10^{-3}	
Lattice Tune	80 degrees	
Depressed Tune	8 degrees	
Lattice Half-Period	8.1 meters	
Focusing Half Angle		33 mrad

Figure 2.49 shows the layout of the final compression and focus. There is a series of three functional sections: a transport section, a compression section, and a transverse focus section. In an alternative layout which we considered, the compression section was located at the end of the linac, so the beam was allowed to compress within the bends. However, with a feasible average bend radius, the tilt removal distance (from Section 2.4.6.2) was not long enough to accommodate bending, spreading, and final focus. The design illustrated in Fig. 2.49 allows the use of a conservative value (51.6 m) for the average bending radius. Also, the chosen layout eliminates the problem of dispersion in the bends due to the large coherent velocity tilt of the compression phase.

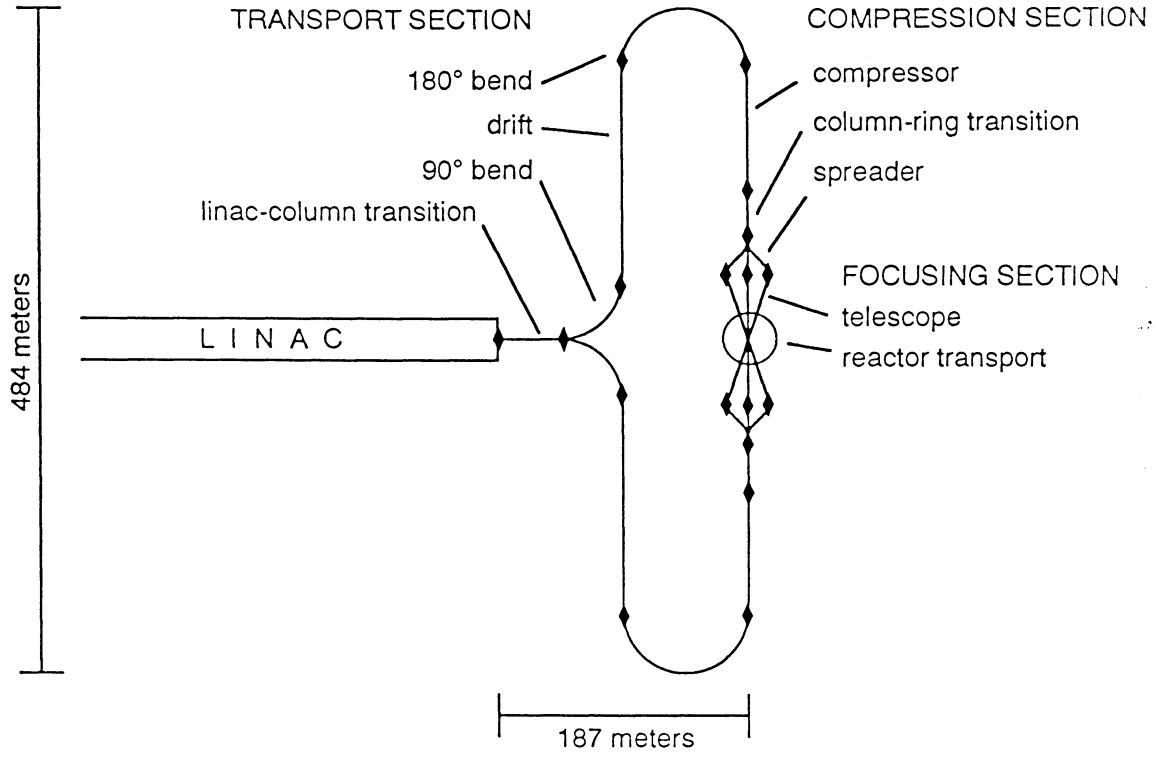

Fig. 2.49. Final compression and focus layout.

Overall design parameters for final compression and focus are listed in Table 2.26. Out of the total of 984 quadrupoles, 624 (from the linac to the compressor) can be made identical to the linac quadrupoles. The total of 528 dipoles includes 24 (2 per beam) which are very low field steering dipoles at the entrance to the reactor chamber. Each of the three functional sections of the final transport systems is now described.

Table 2.26. Overall Final Compression and Focus Design Parameters

PARAMETER	VALUE
Transport Length	611 meters
Linac-to-Target Distance	187 meters
Total Width (⊥ to linac)	484 meters
Number of Quadrupoles - per Beam	984 82
Number of Dipoles - per Beam	528 44

Transport Section. The transport section splits the 12-beam bundle from the linac into two 6-beam bundles, then transports each of the 6-beam bundles so that they are aimed at the target from a sufficient distance to accommodate compression and transverse focus. The transport section is composed of four elements: an initial transition element to transform the 12-beam bundle into two 6-beam columns, a 90 degree bend to direct the columns away from the linac axis, a straight section to carry the columns the required distance from the axis, and a 180 degree bend to direct the bundles back towards the target. Table 2.27 lists key design parameters for each of the transport section elements.

The linac-to-column transition is a translation sequence which is illustrated in Fig. 2.50 a through c. Equal transport lengths for all beams are maintained through this sequence by equalizing the individual lateral translations as indicated. Figure 2.50a shows the close-packed 12-beam rectilinear lattice at the exit to the linac. In Fig. 2.50b, each beam is translated using a dipole to initiate a 0.51 degree bend, followed by 32.1 m drift, then a second dipole, identical to the first but with reversed field, which restores the beam direction at a distance of one beam-lattice spacing from the original beam axis. In total, the transition encompasses two lattice periods (32.4 m).

The result, shown in Fig. 2.50c, is a column of six beams, with the total transport length for each beam exactly the same to this point. The column geometry, with the column

perpendicular to the bend plane, yields automatic equal-length transport through the subsequent major bends. Design parameters for the linac-to-column transition are given in Table 2.27.

Table 2.27. Transport Section Design Parameters.

Element	Linac-column transition	90 degree bend	Straight section	180 degree bend
Transport length	32.4 m	81.0 m	139.3 m	162.0 m
Length (∥ to linac)	32.4 m	51.6 m	139.3 m	103.1 m
Width (⊥ to linac)	0.26 m	51.6 m		51.6 m
Bending radius		51.6 m		51.6 m
Lattice half-period	8.1 m	8.1 m	8.1 m	8.1 m
Lattice tune	80 degrees	80 degrees	80 degrees	80 degrees
Depressed tune	7.0 degrees	7.0 degrees	7.0 degrees	7.0 degrees
Average beam radius	7.3 cm	7.3 cm	7.3 cm	7.3 cm
Dipoles per beam	2	10		20
Length (each)	14 cm	2.4 m		2.4 m
Field	6.7 T	6.7 T		6.7 T
Occupancy	0.8%	30%		30%
Quadrupoles per beam	4	10	18	20
Length (each)	18 cm	18 cm	18 cm	18 cm
Bore	10.9 cm	10.9 cm	10.9 cm	10.9 cm
Conductor field	10 T	10 T	10 T	10 T
Radial gradient	92 T/m	92 T/m	92 T/m	92 T/m
Occupancy	2.2%	2.2%	2.2%	2.2%

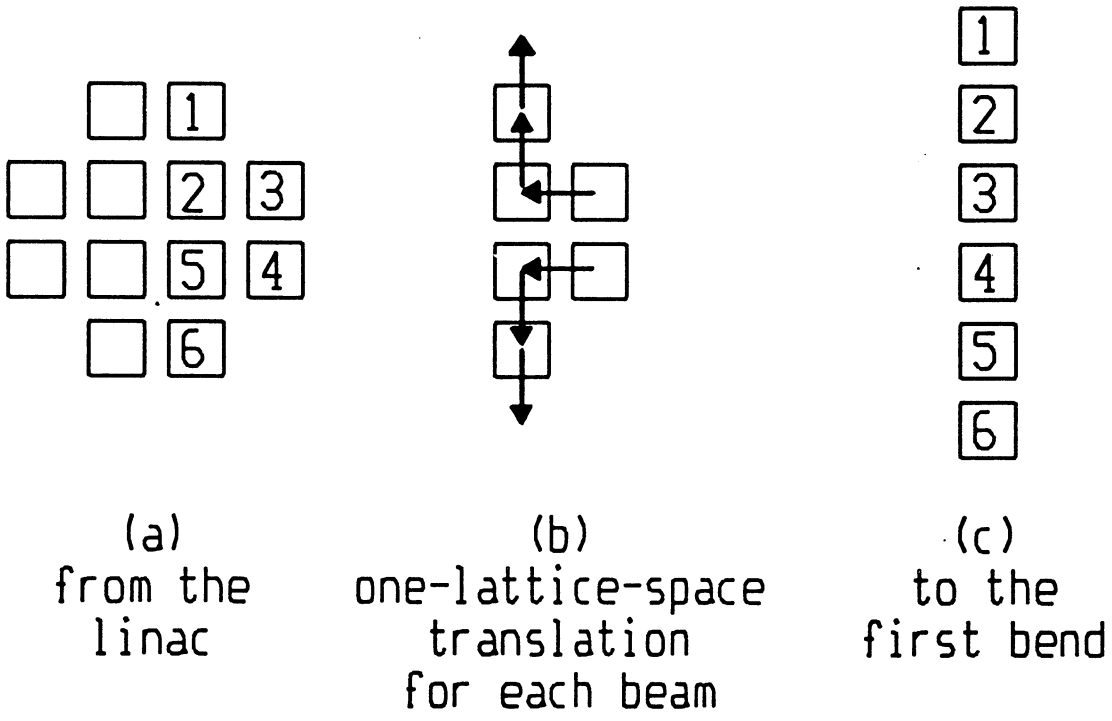

Fig 2.50. Linac-to-column transition.

The 90 degree bend is done by dipole magnets located between the quadrupoles of a FODO focusing lattice with parameters close to those used in the linac. Design parameters for this 5-lattice-period bend are given in Table 2.27. Figure 2.51 displays the calculated bend x and y beam envelopes. This calculation was done with approximate incorporation of space charge, but we would expect a similar result with a rigorous space charge treatment.

The straight section between the major bends is sized to provide the required compression, spreading, and focusing length between the 180 degree bend and the target. Straight section design parameters are given in the table.

The 180 degree bend is designed exactly as two consecutive 90 degree bends. Design parameters are given in Table 2.27. Beam envelopes for each half-bend are shown in Fig. 2.51.

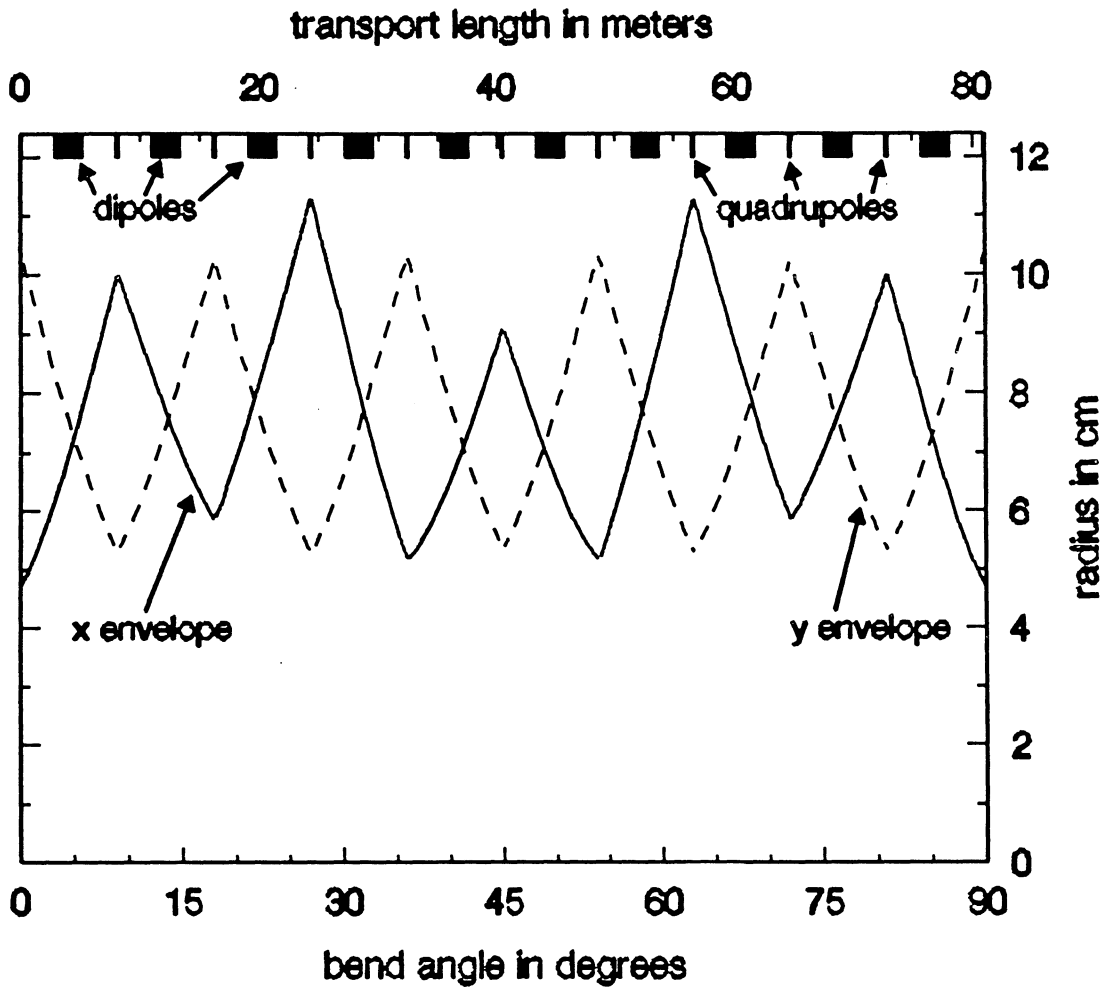

Fig. 2.51. 90 degree bend beam envelopes, quadrupoles and dipoles. (Note horizontal and top vertical scale are very different.)

Compression Section. The compression section provides the specified 10 nsec longitudinal focus in the middle of the final focusing quadrupole set. The compression section is comprised of three elements: the compressor element to provide the required velocity tilt, a transition element to transform the 6-beam column into a hexagonal ring, and a spreading element to provide sufficient clearance between the beams so that the final focusing quads of adjacent beams can be packaged. Table 2.28 lists key design parameters for the compression section elements.

Using the equations in Chapter 2.4.6, a compressor velocity tilt of 5.4% is required to provide the needed factor of 10 in compression. For 3.83 GeV Xe^{+1}, this is a head-to-tail pulse energy spread of 435 MeV. Because no beam acceleration is required from the compressor induction modules (in contrast to the linac), the applied voltage gradient can be relatively high. We chose a maximum of 2.5 MeV/m, which is near the sparking limit for the incoming 100 nsec pulse width. With the gradient ramped from -2.5 MeV/m at the head of the pulse to +2.5 MeV/m at the tail, the required compressor length is 87 meters.

Some beam compression occurs in the induction modules as illustrated in Fig. 2.36. For our baseline system, the equations of section 2.4.6 gave the beam bunch emerging from the compressor a pulse width of 68 nsec. The remaining effective transport length, to the center of the focusing telescope, was then calculated to be 91 meters. Design of the downstream transition element and spreader is constrained to achieve this total.

Pulse shaping to provide a pre-pulse at the target would be done by tailoring the applied voltage gradient waveform in the compressor. This approach allows an arbitrary fraction of the pulse energy to be in the pre-pulse, while preserving the equivalence of the individual beams. No specification on the pre-pulse was available. Additional design parameters for the compressor are given in Table 2.28.

Table 2.28. Compression Section Design Parameters.

Element		Compressor	Column-ring transition	Spreader
Transport length		87.1 m	24.2 m	49.2 m
Length ($\perp$ to linac)		87.1 m	24.2 m	45.2 m
Width ($\parallel$ to linac)				21.2 m
Bending radius				36.9 m
Lattice half-period	L	8.1 → 6.5 m	6.5 → 6.0 m	6.0 → 5.1 m
Bunch length	ℓ	7.3 → 4.9 m	4.9 → 3.0 m	3.0 → 1.6 m
Pulse width		100 → 68 nsec	68 → 41 nsec	41 → 21 nsec
Lattice tune	σ_o	80 degrees	80 degrees	80 degrees
Depressed tune	σ	7 → 6.3 deg	6.3 → 4.9 deg	4.9 → 3.9 deg
Average beam radius	$\bar{a}$	7.3 cm	7.3 → 8.5 cm	8.5→10 cm
Dipoles per beam			2	8
Length (each)			27 cm	2.4 m
Field			6.7 T	6.7 T
Occupancy			2.2%	42%
Quadrupoles per beam		12	4	8
Length (each)		18 → 22 cm	22 → 28 cm	28 → 112 cm
Bore		9.5 cm	9.5 → 10.9 cm	10.9 →15 cm
Conductor field		10 T	10 T	10 T
Radial gradient		92 T/m	92 → 79 T/m	79 →22 T/m
Occupancy		2.2 → 3.4%	3.4 → 4.6%	4.6 → 22%

The transition element that transforms the 6-beam column into a hexagonal ring is a translation sequence which is illustrated in Fig. 2.52 a through c. Equal transport lengths for all beams are maintained through this sequence by equalizing the individual lateral translations as indicated. Figure 2.52a shows the column of six beams emerging from the compressor. In Fig. 2.52b, each beam is translated using a dipole to initiate a 1.0 degree bend, followed by a drift, then a second dipole, identical to the first but with reversed field, which restores the beam direction. In total, the transition encompasses two lattice periods (24.2 m).

The 5.4% velocity tilt will cause the head and tail of the beam bunches to be deflected by different amounts unless the beam translation system is achromatic. Since the deflection of the centroid of the beam is not affected by space charge, designs similar to conventional low intensity achromatic systems can be used. In the column-to-hexagonal-ring transition, the dipole magnets are in the end half-periods of the two-period lattice. A D quadrupole is in the center, and symmetry is maintained about the center. The F quadrupoles adjacent to the bending magnets are tuned to make the translation achromatic.

The result, shown in Fig. 2.52c, is a ring of six beams, with the total transport length for each beam continuing to be exactly the same to this point. Design parameters for the column-to-hexagonal-ring transition are given in Table 2.28.

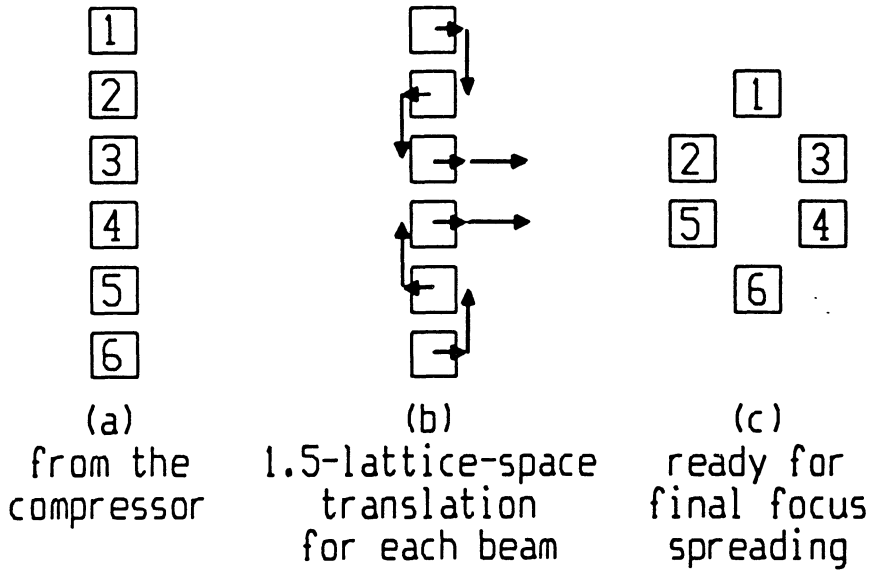

Fig. 2.52. Column-to-hexagonal-ring transition.

The spreader expands the 6-beam bundle to provide sufficient clearance between the beams so that there will be room for the final focusing quads of adjacent beams. The final quadrupoles of the spreader must provide matching to the initial quads of the focusing telescope. Spreader parameters were determined by starting with the required off-axis angle for each of the ring beams as they converge on the target (15.1 degrees), then determining the angles of the two consecutive (and oppositely directed) bends that would both match to the parallel beams emerging from the column-to-ring transition, and would yield the required compressor-to-mid-telescope transport distance to accomplish the longitudinal focus. Symmetry is used to make each of the bends achromatic. Figure 2.53 is a layout drawing of the 6-beam spreader and telescope.

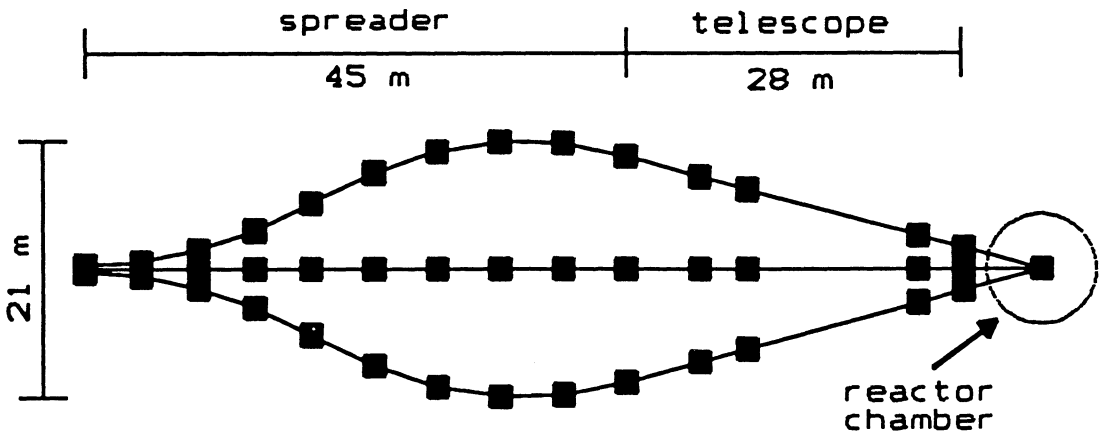

Fig. 2.53. Spreader and telescope layout.

In retrospect, placing the column-to-ring transition before the compression would result in a better design. More length would be allotted to the spreader, resulting in more gradual bending. In addition, smaller and/or fewer induction modules would be needed to surround the ring than would be needed for the 6-beam column.

Transverse Focus Section. The transverse focus section delivers the longitudinally-compressed beam to the target. It consists of two elements: a focusing telescope, which provides the required convergent angle to the beam bunches, and a reactor transport element,

which provides the final beam steering and the auto-neutralizing electrons immediately before the beam bunches enter the reactor chamber. Some combination of shielding, baffles, and shutters at the reactor interface must be included to protect the final focusing components from target radiation, target debris, and hot molten Flibe.

The focusing telescope consists of four quadrupoles. The layout for the 6-beam bundle is illustrated in Fig. 2.53. Figure 2.54 shows the calculated x and y beam envelopes along with the quadrupoles dimensions (shielding is not shown). This envelope calculation and the concurrent specification and placement of the four quadrupoles were done with approximate incorporation of space charge. Note that the horizontal and vertical scales of Fig. 2.54 are far different, so both the beams and quadrupoles are much longer or thinner than they appear in the figure.

The upstream telescope quadrupoles are arranged to keep the beam from converging to a small waist within the telescope, in order to reduce the effect of space charge. However, the beam is small enough that our design would have to be modified to take more accurate space charge design calculations into account, and it may be advantageous to add more quadrupoles to the telescope. A final design would have to take into account chromatic corrections, and also geometrical aberrations in the large diameter quadrupole lenses. This may require sextupole and octupole correction magnets. We would anticipate that incorporation of space charge effects would not lead to major modification of the design.

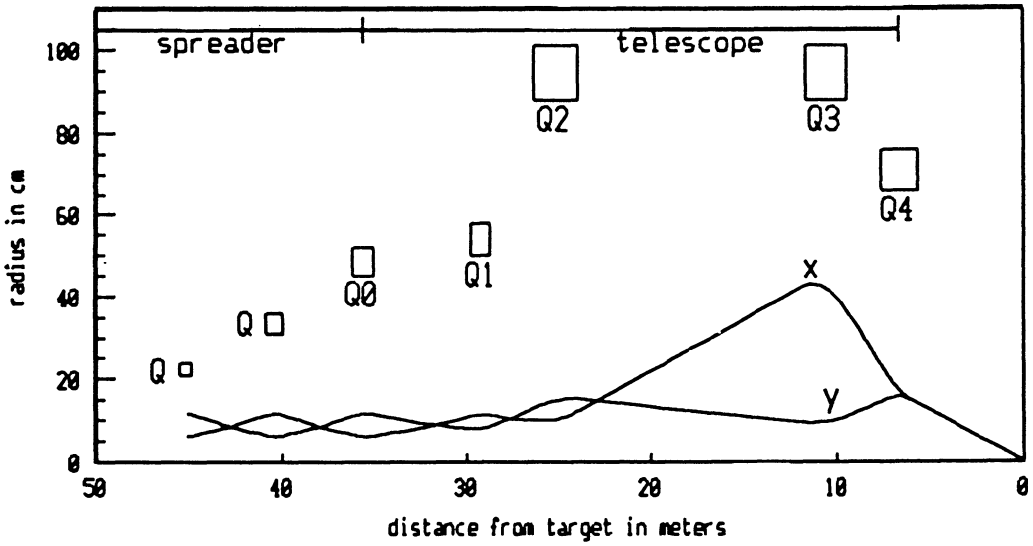

Fig. 2.54. Telescope beam envelopes and quadrupoles.
(Note horizontal and vertical scales are very different.)

Design parameters for the telescope quadrupoles are given in Table 2.29. Bore sizes are driven by radial shielding requirements. Shielding is analyzed and described in Section 2.2.6.6 and is illustrated in Fig. 2.16.

Table 2.29. Focusing Telescope Quadrupole Parameters.

beam →	Q0	Q1	Q2	Q3	Q4 *beam* →	
Distance from Target	35.6	29.2	25.1	10.5	6.6	m
Length	1.12	1.07	2.40	2.17	1.92	m
Shielding I.D.	0.30	0.40	1.12	1.12	0.52	m
Shielding O.D.	0.90	1.00	1.76	1.76	1.32	m
Gradient	-22.3	19.9	-9.5	11.4	-15.2	T/m
Superconductor Field	-10	10	-9.5	10	-10	T

The reactor transport segment is illustrated in Fig. 2.55. Table 2.30 lists geometrical design parameters and focusing performance parameters. The bundle size, as characterized by the bundle-center-to-beam-center angle, is determined in general by the close-packing of either telescope Quadrupole Set 3 or Quadrupole Set 4, depending on their distance from the target and their radial build. For the baseline design, this constraint is at Quadrupole Set 4, although Quadrupole Set 3 is also essentially packed to the limit.

A total of 1.1 m of longitudinal distance was allotted for electron injection and steering dipoles. No electron injector or steering dipole design was done. Although no steering dipole specification was developed, it is known that the beam displacement, and therefore the dipole field, is very small relative to the upstream bending dipoles. The turn-to-turn voltage insulation specification will be very modest, and it is likely that copper windings can be used (which is desirable for fast response). This reduces shielding requirements and allows a relatively small bore, as suggested in the figure. The x and y dipoles would be co-wound to reduce the longitudinal space required.

Because the steering field is very small and the shielding requirements are less than for the telescope quadrupoles, it may even be possible to locate the dipoles within the final quadrupole. The dipoles would displace radial shielding, while serving as shielding themselves. This arrangement provides a very compact, space-efficient layout, but neutronics and ion optics feasibility must be verified.

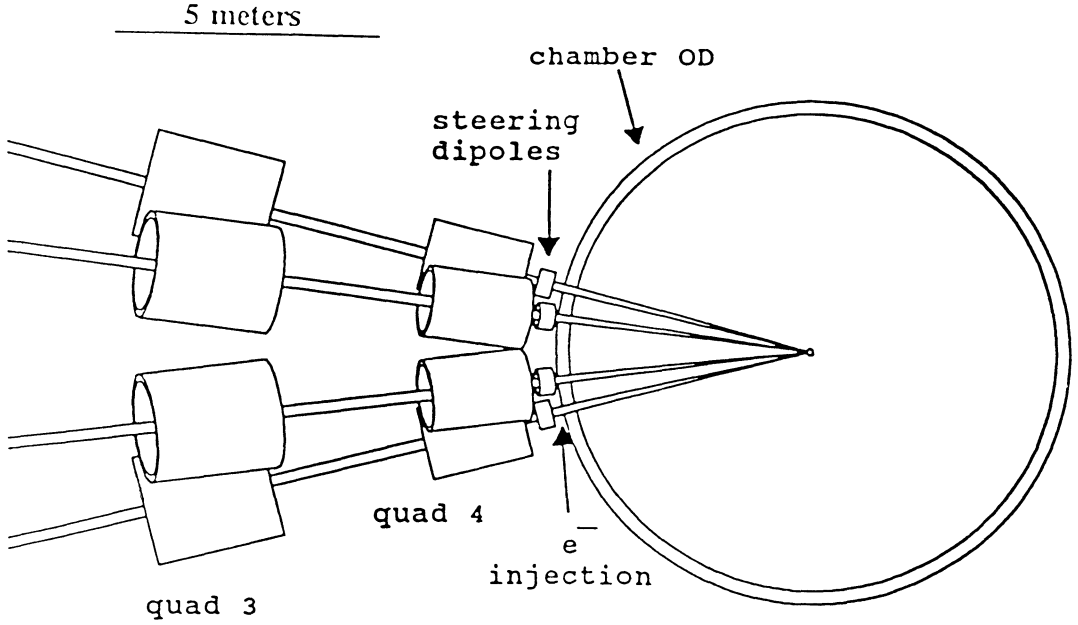

Fig. 2.55. Reactor transport layout.

Table 2.30. Reactor transport design and performance parameters

PARAMETER	VALUE
Vacuum vessel wall O.D.	9.0 meters
Beam geometric convergence half-angle	24.7 mrad
Beam port radius	14.2 cm
Area of beam ports (12 beams)	0.76 m^2
Bundle-center-to-beam-center angle	15.1 degrees
Bundle radius at wall O.D.	1.82 meters
Total wall area for bundles (12 beams)	20.1 m^2
Beam spot radius	2.3 mm
from space charge	1.5 mm
from emittance	1.6 mm
from dispersion	1.3 mm
from jitter/alignment	0.6 mm

2.4.10 Potential Reductions in Driver Cost

2.4.10.1 Low-Energy Transport Driver Savings

Because of the long initial pulse durations dictated by the Child-Langmuir injector limit, low-energy beams require large numbers of cores and quad arrays for small energy gains. Although the low-energy and pulse compression stages of our base driver make up only 8% of the driver length, they require 32% of the core volume and 50% of the quadrupole arrays.

Reducing the initial pulse length would:

- give greater voltage (and therefore energy) changes for a given core size (volt-seconds) and thus reduce the required total core mass, and

- increase the initial voltage gradient allowed by the velocity tilt limit and further reduce the length of the first two driver stages, the required number of quadrupoles, and the required core mass.

Cost/Benefit studies on methods of shortening the initial pulse should be done. An example of an improved base design is given in section 2.4.10.3. The improved driver shortens the initial pulse length by using larger beam sizes early in the driver. Other methods of reducing the initial pulse length could include:

- using higher injected current densities, and

- using beam combination so that more beams are used in the early driver stages than in the high-energy transport stage.

More aggressive source and injector assumptions decrease the estimated driver cost. Injector concepts exist that can provide currents densities above those given by the Child-Langmuir limit. High-performance injector development with more experimental results is needed to determine if savings from improved injectors can be realized.

Beam combination reduces the number of arrays and cores by increasing their sizes. In addition, beam combination leads to beam emittance growth (which degrades target performance as well as increasing bore sizes) and adds uncertainties to driver performance estimates. Further experiments and beam simulations could quantify the emittance growth effects needed to do a cost/benefit analysis for beam combination.

Beam separation before final focusing can lead to smaller spot sizes and higher gains. Beam separation could improve target performance, but improvements will be limited by spot growth resulting from beam combination at the target and by the performance of the beam-

separating magnets. Drivers which use both beam combination and beam separation will have both greater potentials for cost and performance improvements and greater uncertainties in the driver beam quality and achievable target performance.

2.4.10.2 Further Driver Savings

Recirculation. The number of driver components could be significantly lowered by using recirculation, so that the beams could pass through each component several times. Because dipoles used in a recirculating driver must be able to rapidly change the strength of the bending fields to accommodate the changing beam energies, this will require normal bending magnets which will have significant energy loss. Savings from "re-using" components will be offset by the fact that the bore sizes must be set from large initial beam sizes. Furthermore, the bending magnets needed for recirculation add momentum spread to the beams and thus degrade target performance.

Recirculation can be done at any point in the driver, and several recirculating loops may be used in a single driver. A cost/benefit analysis of recirculation should include experimental analysis of the effects of beam bending on beam growth.

Higher Average Voltage Gradients. The length and cost of linear drivers could be reduced if a higher average voltage gradient could be used. The required volt-seconds and core volumes will not change, but the number of quadrupoles and the length of the driver could be reduced. Although average voltage gradients much greater than 1 MV/m have been sustained for very short time periods, more experimental data on high-performance insulator designs is needed before higher average gradients can be assumed for a driver.

2.4.10.3 An Example of Driver Savings for a 5 MJ Driver

The decision to use a single beam radius and only one quadrupole array design allowed us to quickly examine the large available parameter space. The driver design can be improved by using two different quadrupole array designs. Using larger bore quadrupoles in the beginning of the driver will increase the initial beam current and decrease the initial pulse length. Beam compression during the low-energy stage of the driver will allow for smaller quadrupole bores to be used for the high-energy stage, which makes up the majority of the driver. Although the

maximum quad occupancy factor for the improved driver is low (0.5), the half periods early in the driver are short and the quadrupoles are short. The effect of limiting designs to those which use more credible quadrupoles with greater lengths relative to their bores is an area for further investigation.

Figure 2.56 shows how the cost of the quadrupoles and cores of this modified design compares with the same cost subset of drivers using our base-case assumptions. The savings for the quadrupoles and cores for a 5 MJ driver would be approximately $50 M, and the total driver savings (including savings in the pulse forming network, cryogenic system, etc.) would be larger.

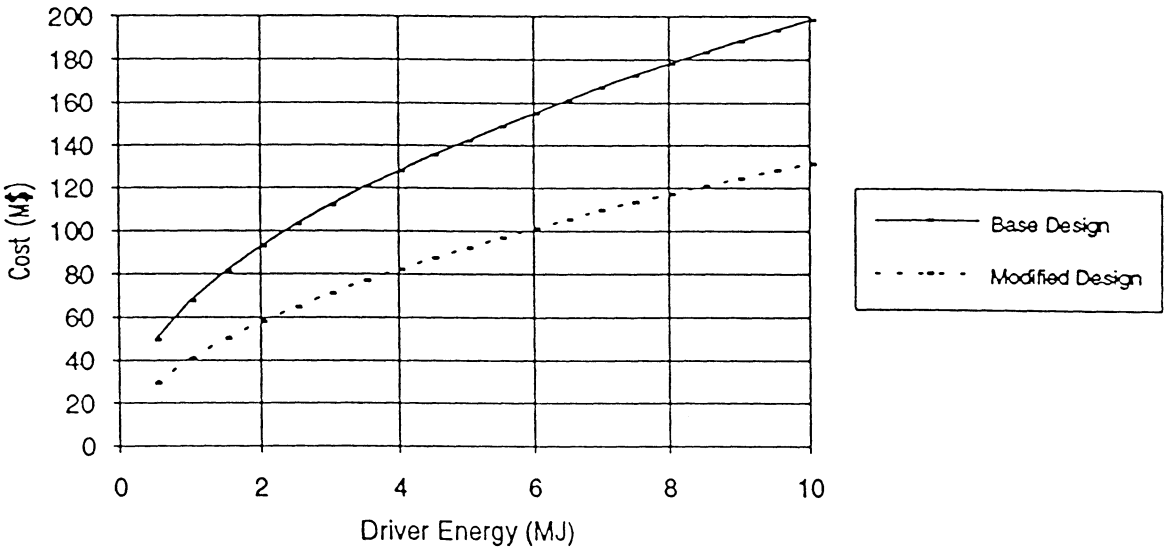

Fig. 2.56. Cost subtotals for modified and base driver assumptions.

2.4.11 Results and Conclusions

The base 5-MJ heavy-ion induction driver we have designed uses conservative design assumptions, has an efficiency of 28% and a cost of only $120/J. Combining the driver efficiency with an estimated target gain of 86.5 gives a recirculating power fraction for a 1,000 MW IFE plant of only ~ 7%. We created a high-performance, low-cost design by

- using an original design for compact arrays of high-performance, Nb_3Sn quadrupoles which leads to small sizes and costs for the inductor cells as well as the focusing arrays, and
- conducting a parametric search over a wide range of possible driver parameters to choose parameters which lead to an attractive design.

We use minimal extrapolation from existing accelerator technology and physics to create highly credible driver performance. We do not use any bends in the accelerator, beam combination, or beam separation. Although driver designs with bends, such as recirculating induction accelerators, offer the potential for cost savings by bending the beams in a circle and reducing the number of required driver elements, present performance uncertainties are large for high-current circular accelerators. Linear driver costs and projected target gains could be improved by combining beams early in the driver and separating them before final focusing; again we avoid performance uncertainties by not using beam combination or separation.

We found significant cost savings by choosing our driver parameters after an extensive search of the allowed driver design parameters. Driver parameters varied in our design sudy were

the number of beams in the driver,

the ion mass,

the ion charge state,

the quadrupole focusing field strength,

the quadrupole spacing, and

the type of superconductor used in the quadrupole windings (Nb-Ti or Nb_3Sn).

We examined the effect of variation in each of these driver parameters on both the driver cost and projected target gain.

By using larger beams early in the driver (and changing our design assumption from one quadrupole array design to two), we were able to further lower the driver cost. Further parametric studies with other design variations could give further savings.

We have developed powerful tools for modeling a wide variety of drivers and identified several areas where these tools could be used to quantify the benefits resulting from more aggressive design options.

2.5 REFERENCES FOR CHAPTER 2

2.1 R.W. Moir, "HYLIFE-II Inertial Confinement Fusion Reactor Design," Lawrence Livermore National Laboratory Report UCRL-JC-103816 (Oct. 1990).

2.2 B. Badger et al., "HIBALL - A Conceptual Heavy Ion Beam Driven Fusion Reactor Study," University of Wisconsin (Sept. 1981).

2.3 B. Badger et al., "HIBALL-II - An Improved Heavy-Ion Beam Driven Fusion Reactor Study," University of Wisconsin Fusion Technology Institute Report UWFDM-625 (Dec. 1984).

2.4 R.R. Peterson, J.J. MacFarlane, and G.A. Moses, "CONRAD - A Combined Hydrodynamic-Condensation/Vaporization Computer Code," University of Wisconsin Fusion Technology Institute Report UWFDM-670 (July 1988).

2.5 J.J. MacFarlane, "IONMIX - A Code for Computing the Equation of State and Radiative Properties of LTE and Non-LTE Plasmas," University of Wisconsin Fusion Technology Institute Report UWFDM-750 (Dec. 1987).

2.6 "T-4 Handbook of Material Properties Data, Vol. 1c: Equations of State," Los Alamos National Laboratory Report LA-10160-MS (Nov. 1984).

2.7 W.J. Moore, *Physical Chemistry*, 3rd ed., Prentice-Hall (NJ) (1965).

2.8 A.E. Scheidegger, *The Physics of Flow Through Porous Media*, 3rd ed., University of Toronto Press (1960).

2.9 R.D. Blevins, *Applied Fluid Dynamics Handbook*, Van Nostrand Reinhold (1984).

2.10 R.A. Greenkorn, *Flow Phenomena In Porous Media*, Marcel Dekker (NY) (1963).

2.11 A.E. Barrington, *High Vacuum Engineering*, Prentice-Hall (NJ) (1963).

2.12 H.S. Carslaw and J.C. Jaeger, *Conduction of Heat in Solids*, Oxford, Clarendon Press (1959).

2.13 F. Kreith, *Principles of Heat Transfer*, International Textbook (1966).

2.14 R.R. Peterson, J.J. MacFarlane, and G.A. Moses, "CONRAD, A Combined Hydrodynamics-Condensation/Vaporization Computer Code," University of Wisconsin Report UWFDM-670 (July 1988).

2.15 J. Heremans and C.P. Beetz, Jr., "Thermal Conductivity and Thermopower of Vapor Grown Graphite Fibers," *Physical Review* B, **32**, No. 4, 1981-1986 (15 Aug 1985).

2.16 R.J. Price, G.R. Hopkins, and G.B. Engle, "Effects of Fast Neutron Irradiation on Carbon Fibers," *Proc. 17th Carbon Conf.*, 348 (1981).

2.17 R.W. Moir et al., "HYLIFE-II Progress Report, Chapter 6," UCID-21816 (1991) and "Blanket Comparison and Selection Study Final Report," Argonne National Laboratory Report #ANL/FPP-84-1, **1** (Sept. 1984).

2.18 W.W. Eagle, Jr., "User's Manual for ANISN," K-1693, Oak Ridge Diffusion Plant (1967).

2.19 R.E. MacFarlane, "TRANSX-CTR): A Code for Interfacing MATXS Cross Section Libraries To Nuclear Transport Codes For Fusion System Analysis," Los Alamos National Laboratory Report LA-9863-MS (1984).

2.20 M. Sawan, W. Vogelsang, and D.K. Sze, "An Effective Penetration Shield Design for ICF Reactors,'' *Proc. 6th International Conf. on Radiation Shielding*, Tokyo, Japan, 675 (May 1983).

2.21 M. Sawan, "Charts for Specifying Limits on Copper Stabilizer Damage Rate," *J. Nucl. Mat.*, **122 & 123**, 1376 (1984).

2.22 W. Maurer, '"Neutron and Gamma Irradiation Effects on Organic Insulating Materials for Fusion Magnets," KfK-3974, Kernforschungszentrum, Karlsruhe (1985).

2.23 M. Sawan and P. Walstrom, "Superconducting Magnet Radiation Effects in Fusion Reactors," *Fusion Technology*, **10**, 741 (1986).

2.24 W.R. Grimes, "Molten Salt Reactor Chemistry," *Nuclear Applications and Technology*, **8**, 137 (1970).

2.25 W.R. Grimes and S. Cantor, "Molten Salts as Blanket Fluids in Controlled Fusion Reactors," in *The Chemistry of Fusion Technology*, D. M. Gruen, Ed., Plenum, New York, 161-190 (1972).

2.26 E.M. Larsen and L J. Wittenberg, "The Chemistry of Molten Li_2BeF_4," *Fusion Technology*, **10**, 990 (1986).

2.27 *J. Phys. Chem. Ref. Data.*, **14**, Suppl. 1 (1985).

2.28 A.B. Chilton, J.K. Schultis, and R.E. Few, *Principles of Radiation Shielding*, Prentice-Hall, Engelwood Cliffs, NJ, 429-431 (1984).

2.29 T.J. Dolan, G.R. Longhurst, and E. Garcia-Otero, "Vacuum Disengager Design for Tritium Removal from HYLIFE-II Reactor Flibe," *Fusion Technology*, **21**, 1947 (1992).

2.30 R.W. Moir et al., "HYLIFE-II Progress Report, Chapter 6," UCID-21816 (1991).

2.31 G.R. Longhurst and T.J. Dolan, "Tritium Permeation Loses in HYLIFE-II Heat Exchanger Tubes," *Fusion Tech.*, **19**, 820 (1991).

2.32 J.L. Anderson et al., "Experience with the TSTA Milestone Runs with 100 Gram-Levels of Tritium," *Fusion Tech.*, **14**, 438 (1988).

2.33 K.B. Woodall, S.K. Sood, and A. Busigin, "Conceptual Design of a Laboratory Scale Impurity Detritiation and Hydrogen Isotope Separation System," *Abstract 4th Topical Meeting on Tritium Technology*, Albuquerque, NM (1991).

2.34 S. Sinharoy, A.R. Keeton, W.J. Lange, "Permeation of Deuterium Through Double Walled Croloy Tubes," Westinghouse Research & Development, Report 86-7B6-HYPER-R1 (June 1986).

2.35 "Development Plan for Advanced Fossil Fuel Power Plants," Electric Power Research Institute, EPRI CS-4029, Final Report (May 1985).

2.36 Craig Fong, Lawrence Berkeley Laboratory, Private communication (October 1991).

2.37 J. Hovingh et al., "Heavy-Ion Linear Induction Accelerators as Drivers for Inertial Fusion Power Plants," *Fusion Technology*, **13**, No. 2, 262 (February 1988).

2.38 W. M. Polansky, "U.S. Accelerator Research Program for Heavy-Ion Fusion," Fusion Technology, **13**, No. 2, 202 (February 1988).

2.39 M. J. Monsler, "The Potential for Reducing the Cost of a Heavy-Ion Accelerator for ICF," Final Report PO #9056305, Submitted to Lawrence Livermore National Laboratory (Feb. 1987).

2.40 E. D. Courant, "Power Transport in Quadrupole or Solenoid-Focusing Systems," *Proc. ERDA Summer Study of Heavy Ions for Inertial Fusion*, LBL-5543, Lawrence Berkeley Laboratory, 72 (Dec. 1976).

2.41 *Fusion Technology*, **13**, No. 2, Special Issue on Heavy-Ion Fusion Systems and Their Assessment (Feb. 1988).

2.42 C.D. Child, *Phys. Rev.*, **32**, 492 (1911).

2.43 R. L. Bieri, "Inertial Confinement Fusion Driver Enhancements: Final Focusing Systems and Compact Heavy-Ion Driver Designs," MIT Nuclear Engineering Ph.D. thesis, Chapters 5 & 6, MIT Press (1991). Also published as Lawrence Livermore National Laboratory Report UCRL-LR-107986.

2.44 R. J. Roark, *Formulas for Stress and Strain*, 3rd Ed., N.Y. McGraw-Hill, 150 (1954).

2.45 S.S. Yu, H.D. Shay et al., "HIF Recirculating Induction Accelerator Report," Lawrence Livermore National Laboratory Report UCRL-LR-108095.

2.46 E. P. Lee, T. Fessenden, and Laslett, *Proc. 1985 Particle Accelerator Conf.*, IEEE Trans. Nucl. Sci., **NS-32**, No. 5, 2489 (1985).

2.47 I. Hoffman, *Applied Charged Particle Optics*, Part C, A. Septier, Ed., Academic Press, 124 (1983).

2.48 E. P. Lee, C. Fong, S. Mukherjee, and W. Thur, "Conceptual Design of Bend, Compression and Final Focus Components of ILSE," *Proc. 1989 IEEE Particle Accelerator Conf.*, Chicago, p. 971.

2.49 E.P. Lee, "Transport of Intense Ion Beams," LBL-21559 (June 1986).

2.50 D.S. Lemons and L.E. Thode, "Electron Temperature Requirements for Ballistically Focused Neutralized Ion Beams," *Nucl. Fusion*, **21**, 529 (1981).

2.51 S. Humphries, Jr., *Charged Particle Beams*, Chapter 11, Wiley, New York (1990).

2.52 J. Hovingh, V.O. Brady, A. Faltens, D. Keefe, and E.P. Lee, "Heavy-Ion Linear Induction Accelerators as Drivers for Inertial Fusion Power Plants," *Fusion Technology*, **13**, 255 (Feb. 1988).

2.53 Attributed to P. Stroud by E.P. Lee, Private communication (March 1990).

2.54 G.H. Gillespie, K. Cheng, and Y-K. Kim, *Proc. Heavy Ion Fusion Workshop*, Argonne National Laboratory Report ANL-79-41 (Sept. 1978).

Chapter 3

SOMBRERO

KrF-laser DrivenPower Plant

CONTENTS